UBVR AND HUBBLE SPACE TELESCOPE MID-ULTRAVIOLET AND NEAR-INFRARED SURFACE PHOTOMETRY AND RADIAL COLOR GRADIENTS OF LATE-TYPE, IRREGULAR, AND PECULIAR GALAXIES[1]

VIOLET A. TAYLOR, ROLF A. JANSEN, AND ROGIER A. WINDHORST

Department of Physics and Astronomy, Arizona State University, Box 871504, Tempe, AZ 85287; violet.taylor@asu.edu,
rolf.jansen@asu.edu, rogier.windhorst@asu.edu

STEPHEN C. ODEWAHN

McDonald Observatory, University of Texas, 1 University Station, Austin, TX 78712; sco@astro.as.utexas.edu

AND

JOHN E. HIBBARD

National Radio Astronomy Observatory, 520 Edgemont Road, Charlottesville, VA 22903; jhibbard@cv.nrao.edu

Received 2005 January 11; accepted 2005 May 10

ABSTRACT

We introduce a data set of 142 mostly late-type spiral, irregular, and peculiar (interacting or merging) nearby galaxies observed in *UBVR* at the Vatican Advanced Technology Telescope (VATT), and we present an analysis of their radial color gradients. We confirm that nearby elliptical and early- to mid-type spiral galaxies show either no or only small color gradients, becoming slightly bluer with radius. In contrast, we find that late-type spiral, irregular, peculiar, and merging galaxies become on average redder with increasing distance from the center. The scatter in radial color gradient trends increases toward later Hubble type. As a preliminary analysis of a larger data set obtained with the *Hubble Space Telescope* (*HST*), we also analyze the color gradients of six nearby galaxies observed with NICMOS in the near-IR (*H*) and with WFPC2 in the mid-UV (F300W) and red (F814W). We discuss the possible implications of these results on galaxy formation and compare our nearby galaxy color gradients to those at high redshift. We present examples of images and *UBVR* radial surface brightness and color profiles, as well as of the tables of measurements; the full atlas and tables are published in the electronic edition only.

Subject headings: galaxies: fundamental parameters — galaxies: interactions — galaxies: irregular —
galaxies: peculiar — galaxies: photometry — galaxies: spiral

Online material: extended figure, machine-readable tables

1. INTRODUCTION

Technological advances such as space-based telescopes like the *Hubble Space Telescope* (*HST*) have expanded our view of the universe to higher redshifts than ever before, giving us the opportunity to look back in time to the earliest stages of galaxy development to determine the mechanisms of galaxy assembly and how galaxies evolved into what we see in the present-day universe. Since the optical and near-IR light of high-redshift galaxies observed with *HST* was emitted in the rest-frame far- to mid-UV ("bandpass shifting"), an understanding of the fundamental UV properties of galaxies in general is crucial to our understanding of these high-redshift galaxies. The vast majority of galaxies in the Hubble Deep Field (HDF) appear to have characteristics resembling local irregular and peculiar/merging galaxies (e.g., Driver et al. 1995, 1998; Glazebrook et al. 1995; Abraham et al. 1996; Odewahn et al. 1996; Ellis 1997), although it is difficult to distinguish these classes at lower linear spatial resolution. Size-luminosity evolution studies show that, at the same luminosity, high-redshift galaxies are more compact and less massive than nearby galaxies, as measured in both the UV and optical rest frames (Giavalisco et al. 1996; Lowenthal et al. 1997; Ferguson et al. 2004; Trujillo et al. 2004). They show that high-

redshift galaxies are inherently different from nearby luminous galaxies, regardless of bandpass shifting effects. Therefore, the resemblance of high-redshift galaxies to nearby lower luminosity irregular and peculiar/merging galaxies may be real, and studying stellar population distributions of nearby irregular and peculiar/merging galaxies may provide further understanding of high-redshift galaxies and hence of galaxy formation and evolution.

Radial color gradients can provide an indication of stellar population or metallicity distribution differences between the inner and outer regions of a galaxy (as modulated by dust) and can constrain certain mechanisms for how a galaxy assembled and subsequently evolved to its present state (Tinsley & Larson 1978; de Jong 1996). There have been several studies of the optical color gradients of sizable samples of nearby field galaxies. These include (but are not limited to) color gradients of early-type galaxies measured by Vader et al. (1988) from 35 elliptical and early-type spiral galaxies in ($B - R$), by Franx et al. (1989) from 17 elliptical galaxies in ($U - R$) and ($B - R$), by Peletier et al. (1990) from 39 elliptical galaxies in ($U - R$) and ($B - R$), and by Tamura & Ohta (2003) from 51 rich galaxy cluster E and S0 galaxies in ($B - R$). All four of these relatively large samples found that elliptical galaxies either become bluer with radius or are constant in color, with color gradients that are generally interpreted as metallicity gradients.

Large studies of later type galaxy color gradients were conducted by several other authors, such as Balcells & Peletier (1994), who measured color gradients from the bulges of 45 early-type spiral galaxies in *UBVRI*. De Jong (1996) determined the color

gradients of 86 face-on spiral galaxies in *BVRIHK*, and Tully et al. (1996) did so for 79 galaxies in the Ursa Major Cluster. Jansen et al. (2000) determined $(U - B)$ and $(B - R)$ color differences between the inner and outer regions of a sample of 196 galaxies of all Hubble types. Bell & de Jong (2000) found stellar population and metallicity gradients for their 121 spiral galaxies, and MacArthur et al. (2004) analyzed color gradients and stellar population and metallicity gradients for these plus 51 other galaxies, including some irregular galaxies. All of these studies confirm the earlier finding (e.g., Sandage 1972; Persson et al. 1979) that spiral galaxies tend to get bluer with increasing radius. These color gradients were found to be mainly caused by stellar population gradients (de Jong 1996; Bell & de Jong 2000; MacArthur et al. 2004). Tully et al. (1996) and Jansen et al. (2000) find that low-luminosity ($M_B > -17$ mag), often late-type/ irregular galaxies are equally likely to become bluer or redder outward. Since there is no plausible galaxy formation theory that predicts positive metallicity gradients (Vader et al. 1988), these redder outer parts are most likely due to stellar age effects or dust. Jansen et al. (2000) find that the low-luminosity galaxies that are bluer in their central regions tend to have strong central Hα emission, supporting the hypothesis that the color gradients in these galaxies are due to a few star-forming regions dominating the local colors. In more luminous massive galaxies, a single star-forming region cannot dominate the azimuthally averaged colors and, hence, the observed color gradients reflect either systematically younger populations or systematically less extinction by dust at larger distances from the center. The presence of a bulge is likely to enhance such color gradients.

Due to significant atmospheric extinction and the poor response of most older thick CCD detectors below the Balmer break, large studies of the near-UV properties of galaxies, especially of the fainter irregular galaxies, which seem to be analogs of the majority of high-redshift galaxies, have not been feasible until the recent advent of large-format UV-sensitive detectors in space, such as on the balloon-borne FOCA telescope (Milliard et al. 1992), sounding rocket and Astro UIT flights (Bohlin et al. 1991; Hill et al. 1992; Kuchinski et al. 2000; Marcum et al. 2001), and *HST* WFPC2 (Windhorst et al. 2002). The overall UV properties of galaxies in general, and of faint late-type galaxies in particular, are still rather poorly understood. Mid-UV and, to a lesser extent, *U*-band data are particularly useful for color gradient analysis: because the UV is more sensitive to changes in age and metallicity, color gradients will be more apparent. A color gradient will be more significant with a longer baseline in wavelength coverage between the two filters used, such that it is most useful to obtain equally deep images in filters at both mid-UV and near-IR wavelengths. Additionally, data at intermediate wavelengths are necessary to properly sample a large range of stellar populations. The high resolution of *HST* mid-UV and *I* images allows us to resolve individual stars or associations, which provides further, more detailed information about the distribution of metallicity and stellar populations within a galaxy. The addition of *H*-band *HST* images removes some of the dust degeneracy in a color analysis, considerably improving stellar population measurements over optical colors alone (Cardiel et al. 2003).

In order to address the deficit of published color gradient studies for a large, homogeneous sample of irregular, peculiar, and merging galaxies across a large range of optical wavelengths, we present a data set of 142 galaxies observed at the Vatican Advanced Technology Telescope (VATT) in *UBVR*. We also present supplemental *HST* mid-UV and near-IR data for six galaxies. We discuss these data sets in § 2 and describe the data analysis in § 3. In § 4 we discuss our results, complementing the

findings of previous studies and increasing the database of color gradients to include a larger sample of irregular and peculiar/ merging galaxies. In § 5 we compare our results to those of the high-redshift universe and discuss possible implications on galaxy formation and evolution.

2. DATA ACQUISITION AND REDUCTION

2.1. *Sample Selection*

We selected 82 galaxies from the RC3 (de Vaucouleurs et al. 1991) with (1) types later than or equal to Sd (de Vaucouleurs type $7 \leqq T \leqq 10$), (2) sizes small enough to comfortably fit within the $\sim 6.'4$ field of view (FOV) of the VATT imager (to ensure accurate subtraction of the sky background), and (3) *B*-band surface brightness[2] brighter than $\mu_B = 25$ mag arcsec^{-2}, to ensure efficient imaging at the VATT and with *HST*. The median diameter of the galaxies in this sample is $\sim 1.'4$, and the median surface brightness is ~ 23.0 mag arcsec^{-2}. We supplemented this sample with 23 galaxies from the list of Hibbard & Vacca (1997), which contains UGC galaxies classified as peculiar or interacting. We imposed the same size and surface brightness criteria while excluding galaxies already imaged by John Hibbard and collaborators. Lastly, for comparison we included 13 earlier type galaxies ($T < 7$) and 24 peculiar or unclassified galaxies that were observed for other projects. The total sample therefore contains 142 galaxies, most of which are irregular or peculiar/ merging.

Figure 1 shows the resulting Hubble type distribution of our galaxy sample. It shows the distribution of types from both the RC3 and our own visual classifications, which are the average of the values assigned to each galaxy by three different observers[3] (V. A. T., S. C. O., S. H. C.) experienced with classifying galaxies. A type of $T = -9$ was assigned to the rare cases where no classification could be determined. Because mergers may play an important role in galaxy evolution via hierarchical galaxy formation models, a type of $T = 14$ was assigned to those galaxies that appeared to be interacting, or in the stages of a merger or postmerger. This extra class was created so that galaxies under the special condition of interactions and mergers could be treated separately. The bottom panel of Figure 1 compares our classifications to those of the RC3, which for the most part agree. Differences between our classifications and those of the RC3 are partially due to galaxies that were unclassified in the RC3 being classifiable from our CCD images. Additionally, our classifiers classified several RC3 irregular types as late-type spiral galaxies. This misclassification in the RC3 is also evident in the *HST* images of Windhorst et al. (2002) and is due to the difficulty of accurately classifying these small, faint galaxies with the photographic plates used for the RC3. These plates had lower spatial resolution, signal-to-noise ratio, and dynamic range than our VATT CCD and *HST* images, such that faint spiral structure may have been missed.

Since most of our sample was chosen from the RC3, biases that are inherent in the RC3 itself will also exist in our own sample. We can test for the consistency of our sample with respect to the RC3 through a comparison between the samples of several quantities. Figure 2 compares the 25 mag arcsec^{-2} *B*-band isophotal diameter (Fig. 2*a*), axis ratio (b/a) (Fig. 2*b*), total *B*-band magnitude (B_T) (Fig. 2*c*), and total ($B - V$) color distributions of the RC3 (Fig. 2*d*) to the measurements for our

---

[2] RC3 total *B*-band magnitude per unit area within the RC3 25 mag arcsec^{-2} *B*-band isophote.

[3] Violet A. Taylor, Stephen C. Odewahn, and Seth H. Cohen; Arizona State University.
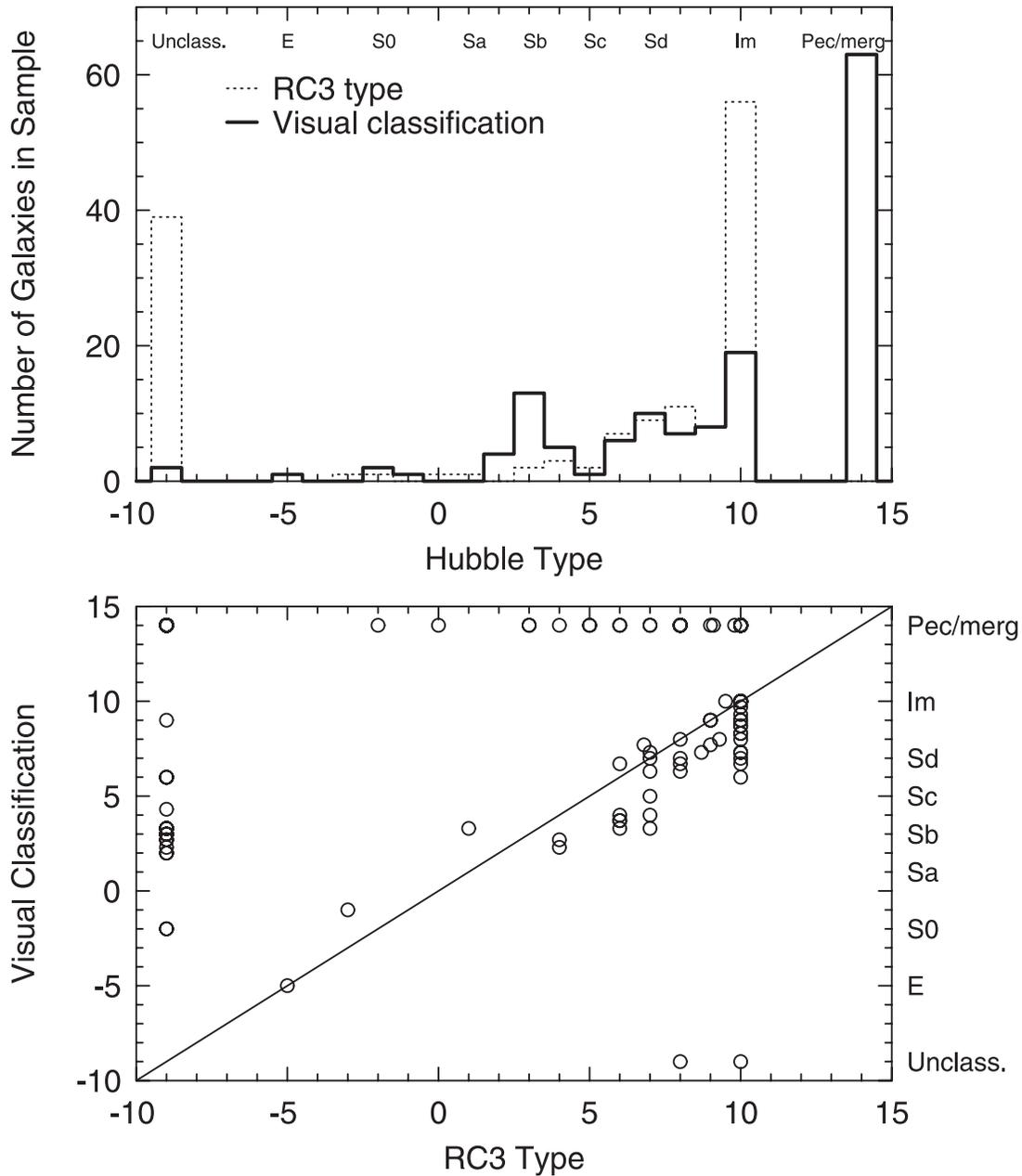
Fig. 1.—*Top*: Distribution of morphological type in our sample of 142 galaxies, using classifications as listed in the RC3 (*dotted line*) and as determined from our VATT R filter images (*solid line*). A numeric type $T = -9$ indicates that no type was given in the RC3, or that it appeared unclassifiable by all of our classifiers. A type of $T = 14$ indicates that our classifiers determined that the object was a strongly interacting galaxy pair, galaxies in the process of merging, or a likely merger remnant. Our sample concentrates on late-type, irregular, and peculiar/merging galaxies. *Bottom*: Comparison of RC3 types to our visual classifications. Several RC3 irregular-type galaxies were classified by our classifiers as late-type spiral galaxies, which may be due to faint spiral structure not being visible in the photographic plates used to classify these small, faint galaxies for the RC3.

sample. Only galaxies with diameters less than the $\sim 6'$ FOV of the VATT CCD are included in Figure 2a. This does not affect the shape of the distribution, since only $\lesssim 1\%$ of the galaxies in the RC3 have diameters larger than $6'$. Our diameter distribution closely resembles that of the RC3. Figure 2b shows that our sample is underrepresented in very flat galaxies, which is to be expected from the deficit of early- to mid-type spiral galaxies in our sample, which are more likely to appear flat when viewed edge-on. Our sample also peaks at a slightly fainter B_T magnitude and a much bluer $(B - V)_T$ color than the RC3 (Figs. 2c and 2d, respectively). This is also to be expected with a late-type galaxy–selected sample because later type galaxies are on average fainter and bluer than earlier type galaxies.

The six galaxies observed with *HST* NICMOS are part of a larger sample of 136 galaxies observed in the mid-UV (F300W) and near-IR (F814W) by WFPC2 (Windhorst et al. 2002; Eskridge et al. 2003; de Grijs et al. 2003), which overlaps significantly with our VATT sample. The entire *HST* data set will be analyzed in more detail in later papers (e.g., V. A. Taylor et al. 2005, in preparation). The *HST* sample was chosen to include galaxies that were predicted to be UV bright and small enough for most of the galaxy to fit within the WFPC2 FOV.

2.2. *Observations*

We obtained our ground-based observations at the VATT at Mount Graham International Observatory (MGIO; Arizona)
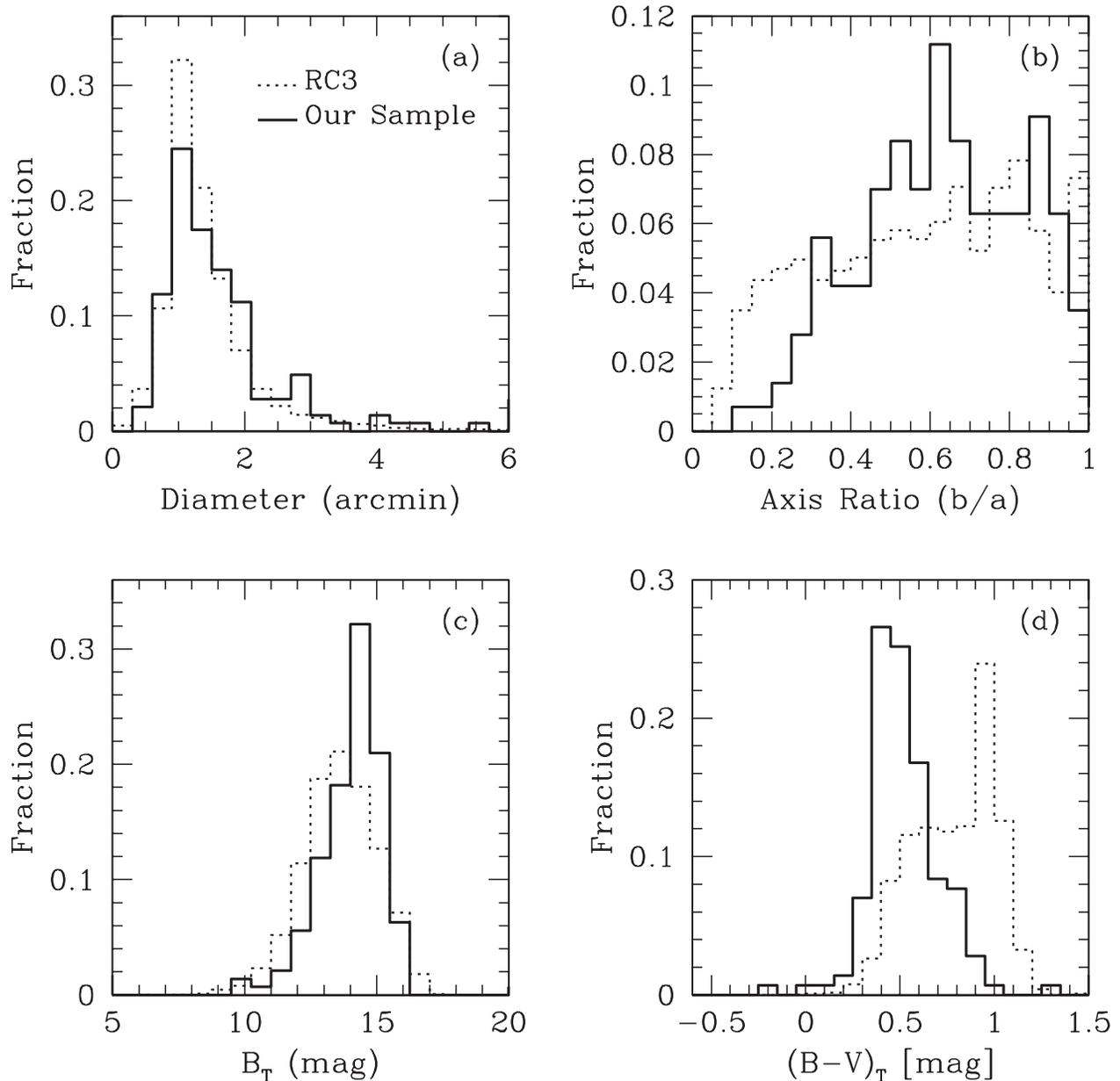
Fig. 2.—Distribution of the (*a*) 25 mag arcsec^{-2} *B*-band isophotal diameter, (*b*) axis ratio (*b/a*), (*c*) total *B*-band magnitude (B_T), and (*d*) total $(B − V)_T$ color of all galaxies in our sample (*solid line*) compared to that in the RC3 (*dotted line*). The diameter distribution of the galaxies in our sample is similar to that of the RC3. Our sample is underrepresented in very flat galaxies, which is expected from the selection effects of our particular sample, since late-type galaxies will not be as flat as earlier type spiral galaxies when viewed edge-on. Our sample peaks at a slightly fainter B_T magnitude than the RC3, which is dominated by more luminous early-type galaxies. The bluer $(B − V)$ color in our sample is the direct result of our selection of UV-bright, late-type galaxies.

with the 2k × 2k Direct Imager because of its high sensitivity in the near-UV, which is critical for our ultimate science goals. The effective quantum efficiency in *U* is ∼40%, which includes transmission loss through the atmosphere combined with the ∼75% transmission of the CCD and the ∼67% transmission of the filter.[4] We binned the CCD images 2 × 2 upon readout, giving a pixel scale of ∼0″375 pixel^{-1}. The typical seeing at the VATT is well sampled by this pixel scale (Taylor et al. 2004). The detector read noise is 5.7e^- and the gain is 1.9e^- ADU^{-1}. Typical exposure times used for the galaxies in our sample were 2 × 600 s in *U*, 2 × 300 s in *B*, 2 × 240 s in *V*, and 2 × 180 s in *R* for galaxies with average total surface brightness brighter than $\mu_B = 24.0$ mag arcsec^{-2} and twice these exposure times for

lower surface brightness galaxies. The long exposure times in *U* and *B* relative to *V* and *R* were chosen to overcome the lower sensitivity and higher atmospheric extinction in these passbands, such that colors within the galaxies can be reliably measured at larger radii before the low surface brightness *U* and *B* light is lost within the sky noise. Observations were spread over nine runs between 1999 April and 2002 April. Photometric nights were defined as those with magnitudes measured for a particular standard star varying no more than 3% throughout the night. During photometric nights, short photometric exposures were taken of galaxies that were observed during nonphotometric conditions.

Table 1 contains a list of all 142 galaxies for which we obtained a full set of calibrated observations in *UBVR*. The full table is available only in the electronic edition. Each galaxy is

---

[4] See http://clavius.as.arizona.edu/vo/R1024/vattinst.html.

TABLE 1
OBSERVED VATT GALAXY LIST

ID (1)	Galaxy (2)	R.A. (3)	Decl. (4)	T_{RC3} (5)	T (6)	Filter (7)	N_{exp} (8)	T_{exp} (s) (9)	sec z (10)	Sky (ADU) (11)	σ_{sky} (12)	μ_{sky} (mag arcsec^{-2}) (13)	Seeing (arcsec) (14)	σ_{seeing} (15)	Observation Date (16)	Photometric? (17)
001............	UGC 00156	00 16 46.30	+12 21 13.1	10.0	9.3	U	2.0	1200.0	1.068	624.654	2.498	20.98	1.554	0.089	1999 Dec 07	n
...	...	...	...	...	...	B	2.0	600.0	1.073	971.057	3.935	21.67	1.470	0.115	1999 Dec 07	n
...	...	...	...	...	...	V	2.0	480.0	1.079	1666.022	13.948	20.65	1.403	0.044	1999 Dec 07	n
...	...	...	...	...	...	R	2.0	360.0	1.069	2230.095	17.548	20.00	1.963	0.153	1999 Dec 08	n
002............	UGC 00404	00 39 19.17	+13 06 40.3	8.0	14.0	U	2.0	1200.0	1.108	654.128	5.195	20.99	1.965	0.119	1999 Dec 07	n
...	...	...	...	...	...	B	2.0	600.0	1.114	1024.339	18.580	21.53	1.680	0.163	1999 Dec 07	n
...	...	...	...	...	...	V	2.0	480.0	1.121	1762.469	18.790	20.73	1.374	0.103	1999 Dec 07	n
...	...	...	...	...	...	R	3.0	360.0	1.064	2195.478	41.374	20.06	2.021	0.186	1999 Dec 08	n
003............	UGC 00512	00 50 02.59	+07 54 55.3	8.0	14.0	U	2.0	1200.0	1.342	740.667	4.676	20.78	1.845	0.077	1999 Dec 07	n
...	...	...	...	...	...	B	2.0	600.0	1.355	1211.626	6.261	21.15	1.813	0.056	1999 Dec 07	n
...	...	...	...	...	...	V	2.0	480.0	1.369	2221.780	23.531	20.54	1.691	0.045	1999 Dec 07	n
...	...	...	...	...	...	R	2.0	360.0	1.103	2380.214	16.848	19.94	1.926	0.133	1999 Dec 08	n
004............	UGC 00644	01 03 16.65	+14 02 01.6	−9.0	14.0	U	2.0	600.0	1.436	328.397	2.273	20.88	1.905	0.175	1999 Dec 05	n
...	...	...	...	...	...	B	2.0	300.0	1.441	549.109	5.125	21.46	2.017	0.103	1999 Dec 05	n
...	...	...	...	...	...	V	2.0	240.0	1.446	961.138	13.536	20.56	1.742	0.047	1999 Dec 05	n
...	...	...	...	...	...	R	2.0	180.0	1.056	993.174	10.910	20.05	1.354	0.102	1999 Dec 06	n
005............	UGC 00749	01 11 30.28	+01 19 10.9	8.0	14.0	U	2.0	600.0	1.186	313.720	1.674	20.98	2.239	0.215	1999 Dec 08	n
...	...	...	...	...	...	B	2.0	300.0	1.188	509.273	6.873	21.83	2.257	0.200	1999 Dec 08	n
...	...	...	...	...	...	V	2.0	240.0	1.190	901.062	11.823	20.61	2.130	0.176	1999 Dec 08	n
...	...	...	...	...	...	R	2.0	180.0	1.173	1032.213	17.354	19.89	1.266	0.153	1999 Dec 06	n
006............	UGC 00849	01 19 23.03	+12 26 57.4	8.0	14.0	U	2.0	1200.0	1.173	555.018	3.437	21.16	2.398	0.625	1999 Dec 05	n
...	...	...	...	...	...	B	2.0	600.0	1.180	941.693	7.004	21.71	2.122	0.065	1999 Dec 05	n
...	...	...	...	...	...	V	2.0	480.0	1.189	1617.641	14.125	20.81	1.879	0.040	1999 Dec 05	n
...	...	...	...	...	...	R	2.0	360.0	1.075	1885.133	17.085	19.97	1.425	0.188	1999 Dec 06	n
007............	UGC 01104	01 32 43.47	+18 19 01.4	10.0	10.0	U	2.0	600.0	1.080	321.698	1.520	20.20	1.860	0.167	2002 Jan 18	n
...	...	...	...	...	...	B	2.0	300.0	1.077	632.436	2.407	20.73	2.092	0.375	2002 Jan 18	n
...	...	...	...	...	...	V	2.0	240.0	1.077	1019.565	4.676	19.81	1.879	0.144	2002 Jan 18	n
...	...	...	...	...	...	R	2.0	180.0	1.076	1320.217	14.134	19.44	1.819	0.148	2002 Jan 18	n
008............	UGC 01133	01 35 00.85	+04 23 11.8	10.0	14.0	U	2.0	1200.0	1.167	572.971	3.850	20.95	1.729	0.104	1999 Dec 04	n
...	...	...	...	...	...	B	2.0	600.0	1.174	941.990	8.528	21.59	1.729	0.154	1999 Dec 04	n
...	...	...	...	...	...	V	2.0	480.0	1.181	1618.724	14.945	20.76	1.521	0.201	1999 Dec 04	n
...	...	...	...	...	...	R	2.0	360.0	1.156	2233.333	25.213	19.42	1.118	0.048	1999 Dec 06	n
009............	UGC 01219	01 44 20.13	+17 28 42.9	−9.0	3.0	U	2.0	600.0	1.068	184.311	0.804	21.27	1.447	0.169	2002 Jan 15	n
...	...	...	...	...	...	B	2.0	300.0	1.065	357.344	1.232	21.63	1.824	0.183	2002 Jan 15	n
...	...	...	...	...	...	V	2.0	240.0	1.064	542.139	1.726	20.94	1.744	0.276	2002 Jan 15	n
...	...	...	...	...	...	R	2.0	180.0	1.063	718.337	1.929	20.14	1.665	0.212	2002 Jan 15	n
010............	UGC 01240	01 46 19.56	+04 15 52.5	8.0	14.0	U	2.0	600.0	1.273	290.342	2.543	21.11	1.991	0.117	1999 Dec 04	n
...	...	...	...	...	...	B	2.0	300.0	1.275	465.680	5.036	21.69	1.901	0.137	1999 Dec 04	n
...	...	...	...	...	...	V	2.0	240.0	1.278	823.495	8.784	20.75	2.070	0.041	1999 Dec 04	n
...	...	...	...	...	...	R	2.0	180.0	1.167	1215.579	14.472	18.73	1.211	0.076	1999 Dec 06	n

NOTES.—Units of right ascension are hours, minutes, and seconds, and units of declination are degrees, arcminutes, and arcseconds. Col. (1): ID number assigned to this galaxy. Col. (2): Galaxy name. Col. (3): Right ascension (J2000.0). Col. (4): Declination (J2000.0). Col. (5): RC3 classification. Col. (6): Visual classification. Col. (7): Filter. Col. (8): Number of images used in each stack. Col. (9): Average exposure time of those images. Col. (10): Average air mass (sec z). Col. (11): Median sky. Col. (12): Uncertainty on a single pixel measurement of the sky. Col. (13): Sky surface brightness. Col. (14): Average stellar FWHM ("seeing"). Col. (15): Uncertainty on the seeing. Col. (16): Observation date of the first deep image combined into the final stack. Col. (17): Whether the individual deep images were photometric: if no ("n"), then the deep images were calibrated with shorter photometric exposures. Table 1 is published in its entirety in the electronic edition of the *Astrophysical Journal*. A portion is shown here for guidance regarding its form and content.

TABLE 2
HST NICMOS and WFPC2 Data Set

Galaxy (1)	R.A. (2)	Decl. (3)	T_{RC3} (4)	r_{outer} (arcsec) (5)	δ_1 (6)	σ_{δ_1} (7)	δ_2 (8)	σ_{δ_2} (9)	δ_3 (10)	σ_{δ_3} (11)
NGC 1311...................	03 20 06.66	−52 11 12.5	9.0	39.44	0.97	0.05	1.42	0.04	0.64	0.03
ESO 418-G008	03 31 30.58	−30 12 46.6	8.0	22.94	−1.05	0.04	−1.26	0.03	−0.26	0.03
NGC 1679...................	04 49 55.31	−31 58 05.5	9.5	33.61	−0.50	0.03	−0.85	0.03	−0.25	0.02
NGC 2551...................	08 24 50.16	+73 24 43.0	0.2	28.56	−2.39	0.03	−2.88	0.03	−0.50	0.01
NGC 3516...................	11 06 47.48	+72 34 06.7	−2.0	25.22	−0.35	0.06	−0.60	0.06	−0.25	0.02
NGC 6789...................	19 16 41.93	+63 58 20.8	10.0	23.51	2.09	0.08	1.87	0.07	−0.32	0.03

Notes.—Units of right ascension are hours, minutes, and seconds, and units of declination are degrees, arcminutes, and arcseconds. Listed are the six galaxies for which we have *HST* NICMOS F160W and WFPC2 F300W and F814W images. Col. (1): Galaxy name. Col. (2): Right ascension (J2000.0). Col. (3): Declination (J2000.0). Col. (4): RC3 classification. Col. (5): Outer annulus radius used in the surface brightness profiles. Cols. (6)–(11): Three color profile slopes and their errors (from the linear least-squares fit) in units of Δmag per r_{outer}, where δ_1 is the slope in (F300W − F814W), δ_2 is the slope in (F300W − F160W), and δ_3 is the slope in (F814W − F160W).

assigned an internal ID number (col. [1]), which we use for brevity throughout the remainder of the paper when referring to a particular galaxy. The average sky background level in each image was determined by taking the median of the median pixel values in 13 120×120 pixel regions along the image border that were relatively devoid of objects. Thus, we minimize contamination by light from the galaxy, which is usually centered within each image. Taking the median values also helps to reject stars, background galaxies, and cosmic rays. Sky gradients have little effect on these sky measurements since, after flat-fielding, the sky background in each image on scales of $\sim 6'$ is flat to better than 1% and typically to $\sim 0.5\%$ in each of the filters. These sky values were used in the reduction process, but local and global sky values were recalculated in a more sophisticated way where appropriate, as described in sections below. Table 1 lists these sky background levels (col. [11]) and corresponding sky surface brightnesses (col. [13]) and seeing estimates (col. [14]) determined from the median stellar FWHM in each image, using the method described in Taylor et al. (2004), where the sky surface brightness and seeing trends in these VATT data are analyzed in more detail.

The near-IR *HST* NICMOS *H*-band data, summarized in Table 2, were taken as part of Cycle 12 SNAP-shot program 9824 (PI: R. Windhorst), using NIC3 in the near-IR (F160W, $\lambda_c = 15500$ Å, or 1.55 μm). Three 500 s exposures were taken of each galaxy. Since NIC3 has a small FOV of 51$\farcs$2, we dithered by about 45 pixels between the three observations to include more of the galaxy in the final mosaic and to facilitate bad pixel removal. The NIC3 detector has a pixel scale of $\sim 0\farcs20$ pixel^{-1}. The *HST* WFPC2 mid-UV (F300W, $\lambda_c = 2992$ Å) and *I* (F814W, $\lambda_c = 8002$ Å) data (see Table 2) were taken as part of Cycle 9 GO program 8645 (Windhorst et al. 2002) or Cycle 10 SNAP-shot program 9124 (PI: R. Windhorst; R. A. Jansen et al. 2005, in preparation). We combined the two separate exposures per filter and the images of all four WFPC2 cameras into a single mosaic. Individual exposures in the mid-UV F300W filter were typically 300–1000 s, while we exposed 40–130 s in *I*. For the Cycle 9 data, the two individual exposures per filter were dithered by ~ 4 pixels to facilitate rejection of bad pixels. The pixel scale in the combined WFPC2 images is $\sim 0\farcs0996$ pixel^{-1}.

2.3. *VATT Data Reduction and Calibration*

The median dark signal (col. [2]) and dark rates (col. [4]) measured in six dark images taken in 2001 April are listed in Table 3. Because these exposures were taken during the day when some sunlight may have leaked onto the detector, they represent an

upper limit of the actual dark current, which may be even smaller. There is an average dark current of 7.54 ± 0.21 ADU hr^{-1}, which results in a worst-case scenario (col. [5]) of 2.51 ± 0.07 ADU in our longest exposure of 1200 s in the *U* band, and which is very small compared to the median *U* sky of 492 ± 12 ADU. If dark current is neglected, this leads to a possible average error in the absolute sky determinations of 0.51% in *U*, 0.16% in *B*, 0.08% in *V*, and 0.05% in *R* (which only matters when finding the absolute sky surface brightnesses and will not affect the galaxy photometry, even to second order). Much larger errors can be introduced through various other uncertainties in the photometry, and subtracting a dark image will only introduce another source of noise without any benefit to the large-scale galaxy surface photometry. Therefore, we did not subtract a dark image or a (likely overestimated) constant dark level from the images.

All images were zero subtracted, flat-fielded, and calibrated with Landolt standard stars (Landolt 1992) using standard methods in IRAF.[5] The photometric zero point for all images is accurate to within $\sim 3\%$. The VATT, at present, does not offer a reliable way of taking dome flats, so only twilight sky flat fields were used. We were usually able to obtain at least three to four good evening sky flats per filter per night and at least another

TABLE 3
Dark Current Measurements

T_{exp} (s) (1)	$\langle$Dark$\rangle$ (ADU) (2)	σ_{dark} (3)	Dark Current Rate (ADU hr^{-1}) (4)	Dark Current (ADU 1200 s^{-1}) (5)
240..............	0.546	3.36	8.18	2.73
240..............	0.525	3.40	7.87	2.62
300..............	0.611	3.54	7.34	2.45
300..............	0.624	3.42	7.49	2.50
600..............	1.131	3.83	6.79	2.26
600..............	1.261	4.08	7.57	2.52

Notes.—Col. (1): Exposure time of the dark image. Col. (2): Total median dark current in the image. Col. (3): Standard deviation on the median dark current. Col. (4): Dark current rate. Col. (5): Dark current corresponding to our longest object exposures of 1200 s taken in the *U* band. Most exposures are much shorter, down to 180 s. It was determined that this dark current is negligible and unnecessary to subtract from object images.
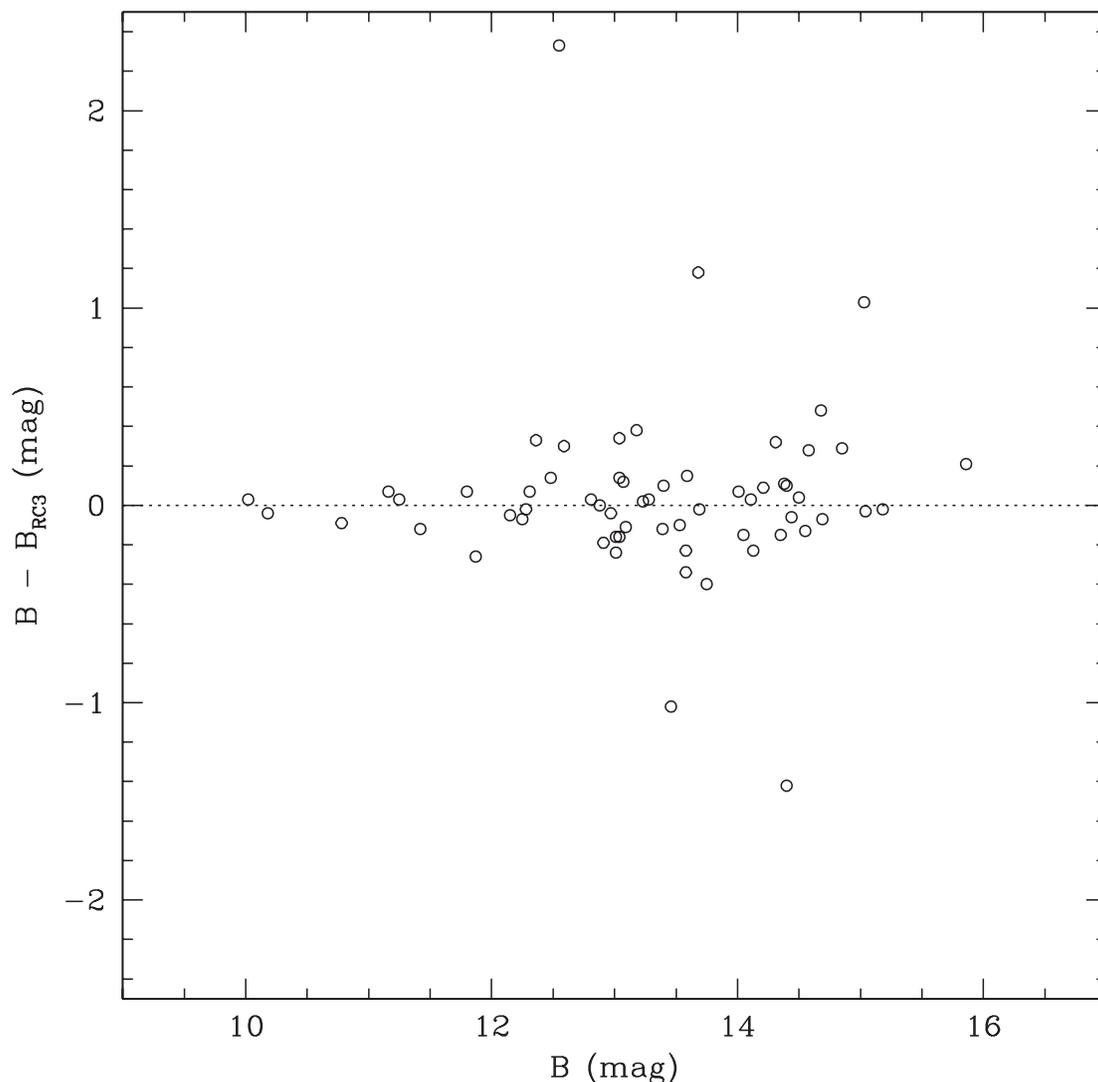
FIG. 3.—Comparison of our calibrated total *B*-band magnitudes to those listed in the RC3, for verifying the consistency of our photometry. Our measured magnitudes tend to agree with those of the RC3 within an average of about 0.2 mag, which is generally comparable to the total magnitude errors quoted in the RC3. There is no significant systematic trend with *B*-band magnitude, which shows that our photometry is consistently accurate for all galaxy brightnesses.

three to four morning sky flats, which sufficed to remove all traces of high-frequency structure. After flat-fielding, at most a 1% gradient in the sky background remained across the entire image. Differences in illumination of the detector between the twilight and night sky, which depend at least in part on the position of the telescope relative to the Sun and Moon, appear to be the cause. Because this gradient is less than 1% across the entire image and because most of our galaxies are ∼1′ in size and centered in the exposure, galaxy photometry will be only slightly affected by this gradient, especially when compared to other larger sources of uncertainty. A 1% error in the sky corresponds on average to 27.0, 27.5, 26.5, and 26.0 mag arcsec^{-2} in *U*, *B*, *V*, and *R*, respectively (as calculated from the average sky brightnesses presented in Taylor et al. 2004), which is fainter than the level at which our surface brightness profiles are reliably determined and therefore should have little effect on our results. Therefore, sky gradient corrections were not applied.

Individual galaxy images were combined on a per-filter basis with integer pixel shifts. This is sufficient for our purposes because the seeing is oversampled (with 4–5 pixels per FWHM, on average) and because this analysis focuses on large-scale radial trends. We also normalized the images to an exposure

time of 1 s, air mass of 1, and zero point of 25 mag arcsec^{-2}, for convenience. To verify the consistency of our photometry, we present a plot of the difference between our measured total *B*-band magnitudes and those from the RC3 versus our measured total *B*-band magnitudes in Figure 3. Our values agree with those of the RC3 within an average of 0.2 mag, which is comparable to the total magnitude errors quoted in the RC3. There is no significant systematic trend with total *B*-band magnitude, which shows that our photometry is consistently accurate for the full range of galaxy brightnesses.

Cosmic rays were removed using an IRAF script by Rhoads (2000), which rejects cosmic rays based on filtering out the point-spread function (PSF) minus a user-scaled delta function and rejecting any objects below a defined threshold to remove those objects that are much sharper than the PSF and therefore cannot be real objects. The input parameters were modified by hand on a galaxy-per-galaxy basis to avoid erroneously rejecting pieces of the target galaxy. Any remaining cosmic rays were masked manually and interpolated over.

The images were astrometrically calibrated using LMORPHO (Odewahn et al. 2002), which calculates approximate astrometric solutions from user-interactive comparisons of several stars in

the target image to the same stars in a DSS[6] image of the same region. It then refines the solutions by comparing all objects found with SExtractor (Bertin & Arnouts 1996) in the target image to accurate positions for all objects in this region listed in the USNO-A2.0 catalog (Monet et al. 1996).

In order to obtain matched aperture photometry so that galaxy properties in different passbands can be directly compared to one another, the images in each filter were all registered with LMORPHO to the V band, which was chosen as the reference passband because it typically has high signal-to-noise ratio and few saturated stars. The SExtractor object lists were compared between filters to find linear shifts, and the images were shifted accordingly.

Finally, nontarget objects were replaced with a local sky value ("patched") using LMORPHO, which uses positions from the object list created by SExtractor and a user-defined threshold value to patch out a large enough area to remove most of the light from each unrelated neighboring object. Each image was reviewed interactively to remove the target galaxy from the patch list and to add any objects that SExtractor missed. In the case of interacting galaxies, the target was treated separately and the companion galaxy patched out unless there was no clear way to distinguish the galaxies, in which case they were treated as one. The patched area was replaced with an average value for the local sky that LMORPHO determined through an iterative sky-mapping procedure, which rejects objects above a certain signal-to-noise ratio threshold level.

2.4. *HST Data Reduction and Calibration*

Combined images of the *HST* WFPC2 mid-UV F300W and near-IR F814W observations were obtained as type B associations from the Space Telescope Science Institute (STScI) data archive.[7] The associations were then mosaicked using WMOSAIC within the STSDAS package in IRAF.

The individual *HST* NIC3 F160W images were combined with CALNICB within the STSDAS package in IRAF, using shifts found semiautomatically with IMCENTROID. We used the VEGA zero point of 21.901 mag arcsec^{-2} for the NICMOS data, calculated from the calibration data presented on the NICMOS Web site at STScI.[8] Some bad pixels that were not removed with the pipeline bad pixel mask were removed by hand.

The WFPC2 images were registered to the NICMOS images by manually finding the coordinates of stars in common between images in each field and by using these in GEOMAP and GEOTRAN in IRAF to apply the proper transformations. Nontarget sources in all images were patched within LMORPHO to an average local sky value using the same method as with the VATT data. We adopted the Holtzman et al. (1995) zero points for each WFPC2 image.

3. DATA ANALYSIS

3.1. *Surface Brightness Profiles*

Surface brightness profiles were calculated with LMORPHO for each galaxy within 12 equally spaced elliptical annuli, start-ing from the galaxy center. Parameters such as galaxy center, annulus radius, axis ratio, and position angle were chosen to match the shape of the outer isophotes and were fixed in the R band for the VATT data and the NICMOS F160W band for the *HST* data. These were then applied to all other passbands in order to achieve matched aperture photometry that could be directly and consistently translated into a color profile. The random error was calculated for the surface brightnesses with the formula

$$\sigma = \sqrt{\frac{\sigma_{\mathrm{sky}}^2}{N} + \frac{\langle F \rangle + \langle \mathrm{sky} \rangle}{N}}, \qquad (1)$$

where $\langle F \rangle$ is the measured average flux per pixel above sky within the annulus and N is the number of pixels in the annulus. This does not include systematic errors due to small sky subtraction errors, which can result in significant errors in the galaxy surface brightnesses as calculated at large radii, making the last few points in the surface brightness profiles less reliable than the inner points. Because the FOV in the VATT images (6′.4) is much larger than the size of most of the galaxies (diameter ∼1′) and because the fields tend to be uncrowded at high Galactic and ecliptic latitudes, we expect few objects to contaminate the VATT sky determinations. Errors due to the small (≲1%) gradients in the sky tend to drop out in the ellipse fitting, as long as the background shows no higher order structure. The *HST* NICMOS data, however, have a much smaller FOV (51″.2). Therefore, it is much more difficult to obtain sky values in the *HST* images that are not contaminated by the galaxy, and as such the points in the outer part of the *HST* profiles are less reliable than those in the VATT profiles. These larger uncertainties in the outer profile points are accounted for when determining color gradients, as described in § 3.2, such that they will have minimal impact on the accuracy of our final results.

Figure 4 shows a comparison of our VATT surface brightness profiles in *UBR* to those of Jansen et al. (2000), for the six galaxies in common between our samples. For this comparison, our major-axis radii, r, were converted to *elliptical* or *equivalent* radii, $r_{\mathrm{ell}} = r(b/a)^{1/2}$. The solid lines represent an estimate of the average 1 σ error found by adding our errors in quadrature with those of Jansen et al. (2000). For the most part, both of our profiles agree within the uncertainties, with a few slightly deviant points that can be attributed to various differences in the way that the two profiles were created. Jansen et al. (2000) applied a color term correction to each annulus separately, while we applied a single color term to the entire galaxy, based on its overall average color. The color term correction is small and difficult to measure accurately without a large number of standard stars of all colors taken throughout each observing night (which would sacrifice significant galaxy observing time). Therefore, errors introduced by using the average color of a galaxy to determine an average color term will be small compared to the errors inherent in measuring the small color term correction and will therefore have little effect on our results. In extreme cases, this will cause the profiles to vary only slightly, if the galaxy color is a significant function of radius. Larger deviations in color gradient measurements are introduced by different choices of the galaxy center, as well as its axis ratio and position angle, which is especially an issue for galaxies with irregular or peculiar morphologies. For these morphologies, the choice of center is somewhat subjective, and the brightest peak often does not coincide with the center of the outer parts or disk. That center, as well as the shape and orientation of the isophotes, can vary significantly

---
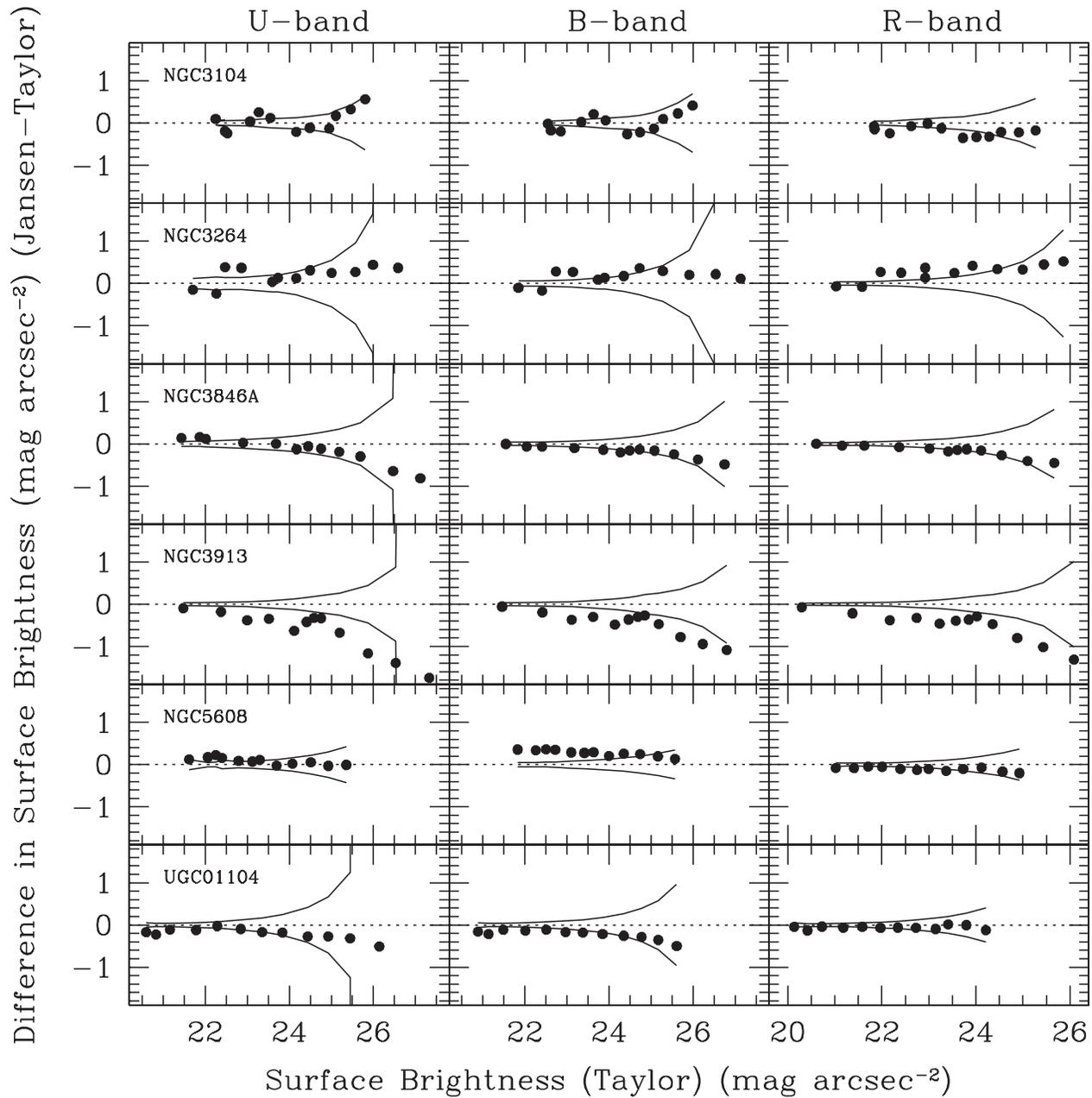
FIG. 4.—Difference in surface brightnesses ($\Delta\mu$) at particular radii as a function of surface brightness μ for six galaxies previously observed by Jansen et al. (2000). The difference is in the sense of Jansen et al. (2000) minus our profile, and the abscissa reflects our measurements of μ. As an aid in distinguishing significant differences, the solid lines indicate 1 σ deviations, computed as the quadratic sum of the errors in the individual profiles. Deviations from zero in the inner parts of the galaxies result most frequently from a different choice of center, position angle, and/or axis ratio, causing different morphological structures to be sampled. Deviations in the outer parts are dominated by sky subtraction uncertainties. For the most part, both profiles agree to within the uncertainties, typically a few tenths of a magnitude. The galaxy showing the poorest agreement, NGC 3913, is asymmetric with significant spiral structure, causing differences in assumed shape and orientation to have a large impact. The position angles adopted here and in Jansen et al. (2000) differ by over 50°, which could account for the relatively large discrepancies.

with radius. This effect can lead to vast differences in the choice of axis ratio and position angle, depending on how the observer chose to define them. In our case, these parameters were calculated automatically by LMORPHO and then inspected manually, with a few values tweaked to change the center, ellipticities, and position angles from the brightest uncentered peak to the center and shape of the outer disk. The choice of these parameters has the largest effect on the inner parts of the profiles, where a change in adopted axis ratio and orientation may result in different structures within the galaxy being sampled. The outer parts of the profile will be more dominated by sky subtraction errors. No attempt was made to correct for

choice of the galaxy center, axis ratio, or position angle for this comparison.

Our profiles generally agree with those of Jansen et al. (2000) within a few tenths of a magnitude, which is similar to the differences they found in comparing their profiles with several other independent observers. The galaxy with the largest disagreement between our and the Jansen et al. (2000) profiles is NGC 3913, which is an asymmetric spiral galaxy. This asymmetry makes the choice of position angle and axis ratio particularly important, such that small changes in either could have a significant effect on the surface brightness profile. Jansen et al. (2000) used an axis ratio (b/a) of 0.9333 and a position angle (P.A.) (east of north) of

$165°$, compared to our b/a of 0.967 and P.A. of $38°.4$, which could account for the relatively large discrepancy in our surface brightness profiles.

3.2. *Color Profiles and Radial Color Gradients*

Radial color profiles were calculated from the surface brightness profiles. The errors on the color profiles were calculated by adding the independent errors of the surface brightnesses profiles for each of the two filters (see eq. [1]), converted to units of mag arcsec^{-2}, in quadrature. Using units of mag arcsec^{-2} is adequate, since the error on the flux, σ, will be small, and the error on the magnitude, σ_μ, is related to the error on the log of the flux, $\sigma_{\log f}$, by

$$\sigma_\mu = 2.5\sigma_{\log f} = 1.0857\frac{\sigma}{f} \approx \frac{\sigma}{f}. \qquad (2)$$

To measure the extent to which the VATT color profiles are becoming redder or bluer with increasing radius (color "gradient" or "slope"), we applied a linear least-squares fit to the color profiles outside of the half-light, or *effective*, radius, r_e (as calculated from the R-band surface brightness profile), for the outer disk components, and separately applied a fit inside of r_e for the inner parts, which may be more affected by a bulge component, if present. Points where the measured average flux per pixel was smaller than $0.5\sigma_{\rm sky}$ were not included in the fit in order to ignore values that have large uncertainties due to low signal-to-noise ratio. To obtain more reliable color gradients, we weighted the points on the color profile by their errors. All radii were normalized to the effective radius in order to allow comparison of galaxies with various sizes. Therefore, our adopted units for the color profile slopes are the change in color (Δmag) per unit effective radius (r_e), where a positive slope indicates that a galaxy is getting redder with increasing radius from its center, and a negative slope indicates that it becomes bluer outward. If there were fewer than three good points in the inner or outer region of a galaxy, no slope was calculated for that region. Table 4 lists the outer color slopes (gradients) measured for all 142 galaxies (cols. [16]–[19]), as well as some other measured quantities such as effective radius (in both angular [col. (3)] and linear [col. (4)] units), total apparent and absolute B magnitudes (cols. [7] and [8]), average B surface brightness within r_e (col. [12]), and total (cols. [9]–[11]) and effective $(U - B)$, $(B - V)$, and $(V - R)$ colors (cols. [13]–[15]), where the effective color is defined as the average color within r_e. The entire table for all of the galaxies is provided only in the electronic version. Figure 5a shows the first few VATT surface brightness and color profiles with their fits. The rest of the profiles are shown only in the electronic edition.

Due to the small FOV of the *HST* images and the low signal-to-noise ratio at low surface brightness levels, the outermost parts of the galaxies are not necessarily detectable in the *HST* images, and it is thus not feasible to measure r_e from their surface brightness profiles. Therefore, we measured all *HST* color gradients across the entire galaxy profile, such that the units for the slopes are change in color (Δmag) per $r_{\rm outer}$, where $r_{\rm outer}$ is the radius of the outermost annulus used in the surface brightness profile (which was defined to go out far enough to include most of the light visible in the F160W image). When the signal-to-noise ratio was too low to reliably determine a surface brightness in an annulus, a surface brightness was not calculated for that annulus and not included in the color slope calculation. The remaining points were weighted by their errors, except for the innermost point of NGC 3516, which was eliminated from the fit

because the galaxy's center is saturated in the WFPC2 images. The color gradients measured from the *HST* F300W, I, and H surface brightness profiles are listed in Table 2.

4. RESULTS

4.1. *VATT* $(U - R)$ *Radial Color Gradients*

Figure 6 shows examples of the surface brightness and color profiles for a few VATT galaxies with notable radial color gradient trends, along with images of the galaxies in U and R with ellipses marking the outer annulus used to calculate the final point in the surface brightness profiles. NGC 4476 is an early-type galaxy ($T = -1.0$) with no significant radial color gradient, although it does become slightly bluer with radius. UGC 04095 is a mid-type spiral galaxy ($T = 6.0$) that becomes similarly slightly bluer with increasing radius. UGC 01104 and UGC 00156 are late-type galaxies ($T = 10.0$ and 9.3, respectively) that become redder with increasing radius. UGC 01104 and UGC 00156 differ in that UGC 01104 gets redder with increasing radius throughout (in the inner parts [$r < r_e$] and the outer parts [$r > r_e$]), while UGC 00156 gets bluer with radius in the inner parts ($r < r_e$) and redder in the outer parts ($r > r_e$). This flip in color slope sign is common, occurring in about half of our galaxies.

The slopes of the outer "disk" ($r > r_e$) $(U - R)$ color profile fits measured in our VATT images are plotted versus Hubble type, total absolute B magnitude, r_e in kpc (for $H_0 = 71$ km s^{-1} Mpc^{-1}), and axis ratio (b/a) in Figure 7. The $(U - R)$ color is shown because it provides the largest wavelength baseline, but the same trends are seen in all other possible $UBVR$ color combinations. The color slope is zero if there is no change in color with radius, positive if the galaxy becomes redder at larger radii, and negative if the galaxy becomes bluer at larger radii. An error bar in the top left panel shows the representative median uncertainty on the $(U - R)$ color gradient slopes, as derived from the linear least-squares fit. Median color slopes for several type bins are plotted by open triangles on top of the individual data points in the Hubble type plot. Boxes surrounding each median value enclose the type bin and the color slope 25% and 75% quartile ranges. Vertical error bars on these points indicate the error on the median (T50), which is calculated from the 25% (T25) and 75% (T75) quartile values with

$$\sigma_{\rm T50} = \frac{1.483({\rm T75} - {\rm T25})}{2\sqrt{N - 1}}. \qquad (3)$$

The median color slope becomes larger (redder with increasing radius), and the overall scatter, or range of possible color slopes, increases with later Hubble types, less luminous total magnitudes, smaller effective radii, and, to a lesser extent, rounder axis ratios. This similarity in trends is not surprising, since all of these parameters are not entirely independent, with later Hubble type galaxies tending to be fainter, smaller, and sometimes rounder than earlier type galaxies, with disks that are less rotationally supported.

The median color gradients in the plot of slope versus Hubble type (Fig. 7) show that galaxies with types E through S0 have no significant radial color slope within the 1 σ error on the median (-0.02 ± 0.03 mag arcsec^{-2} per r_e) or at most a very slight negative slope that would indicate a weak trend of bluer colors with increasing radius. Although this is determined from small number statistics (four galaxies), it is consistent with the findings from other studies of elliptical galaxy color gradients (Vader et al. 1988; Franx et al. 1989; Peletier et al. 1990). There

TABLE 4
VATT Measured Galaxy Parameters

ID (1)	D_{24} (arcsec) (2)	r_e (arcsec) (3)	r_e (kpc) (4)	b/a (5)	V_{GSR} (km s^{-1}) (6)	B_T (7)	B_T (abs) (8)	$(U-B)_T$ (9)	$(B-V)_T$ (10)	$(V-R)_T$ (11)	μ_e (B) (12)	$(U-B)_e$ (13)	$(B-V)_e$ (14)	$(V-R)_e$ (15)	$\delta(U-R)/r_e$ (16)	$\delta(U-B)/r_e$ (17)	$\delta(B-V)/r_e$ (18)	$\delta(V-R)/r_e$ (19)
001......	95.61	26.88	2.33	0.540	1267.	14.580	−16.678	−0.083	0.576	0.394	23.150	−0.083	0.691	0.379	0.180	0.125	−0.112	0.157
	...	...	...	...	...	0.024	0.064	0.037	0.032	0.029	0.027	0.043	0.037	0.034	0.159	0.171	0.118	0.105
002......	51.13	14.90	10.93	0.460	10742.	15.836	−20.063	0.050	0.362	0.374	22.895	−0.179	0.405	0.374	0.251	0.364	−0.074	−0.048
	...	...	...	...	...	0.041	0.071	0.064	0.057	0.055	0.047	0.072	0.066	0.066	0.251	0.266	0.202	0.189
003......	45.74	10.60	3.98	0.770	5496.	14.966	−19.478	0.065	−0.004	0.640	21.986	0.065	0.185	0.636	−0.174	0.039	−0.476	0.323
	...	...	...	...	...	0.024	0.064	0.038	0.036	0.034	0.031	0.047	0.048	0.048	0.084	0.088	0.105	0.100
004......	58.99	10.85	...	0.420	....	15.382	...	0.063	0.662	0.652	21.836	0.158	0.760	0.780	0.395	0.079	−0.072	0.444
	...	...	...	...	...	0.023	...	0.038	0.030	0.023	0.036	0.055	0.050	0.049	0.119	0.136	0.073	0.053
005......	85.13	12.65	5.94	0.280	6882.	14.560	−20.372	−0.678	0.653	0.285	20.949	−0.790	0.765	0.441	−0.050	0.048	−0.035	−0.054
	...	...	...	...	...	0.013	0.061	0.017	0.017	0.016	0.031	0.045	0.045	0.047	0.025	0.027	0.029	0.027
006......	58.12	11.49	11.31	0.620	14410.	14.805	−21.732	−0.081	0.572	0.532	21.686	−0.072	0.677	0.532	−0.083	0.093	−0.109	−0.068
	...	...	...	...	...	0.019	0.062	0.029	0.025	0.022	0.028	0.040	0.039	0.039	0.046	0.052	0.046	0.038
007......	72.83	13.39	0.71	0.610	775.	14.507	−15.683	−0.153	0.533	0.448	21.393	−0.333	0.413	0.364	0.569	0.298	0.188	0.120
	...	...	...	...	...	0.019	0.062	0.028	0.026	0.023	0.029	0.042	0.040	0.038	0.089	0.098	0.067	0.059
008......	26.98	14.53	2.02	0.920	2031.	14.684	−17.598	−0.432	0.077	−1.138	22.973	−0.310	0.204	−0.690	...	−0.134	−0.202	...
	...	...	...	...	...	0.081	0.100	0.113	0.126	0.233	0.051	0.070	0.082	0.256	...	0.660	0.697	...
009......	81.79	10.43	3.35	0.530	4708.	13.718	−20.390	0.178	0.709	0.592	20.871	0.488	1.102	0.957	−0.157	−0.050	−0.063	−0.042
	...	...	...	...	...	0.009	0.060	0.015	0.011	0.009	0.022	0.030	0.034	0.039	0.016	0.018	0.014	0.010
010......	67.98	11.07	1.41	0.300	1862.	15.102	−16.992	−0.324	0.401	0.173	21.136	−0.203	0.401	0.301	−0.495	−0.262	−0.033	−0.205
	...	...	...	...	...	0.019	0.062	0.026	0.026	0.032	0.037	0.051	0.053	0.059	0.203	0.170	0.163	0.198

Notes.—Col. (1): Galaxy ID number assigned in Table 1. Col. (2): R-band 24th magnitude isophotal diameter. Col. (3): R-band effective radius within which half of the light is contained in arcseconds. Col. (4): Radius r_e in kpc using $H_0 = 71$ km s^{-1} Mpc^{-1}. Col. (5): Axis ratio. Col. (6): RC3 Galactic standard of rest velocity. Col. (7): Total B-band apparent magnitude derived from extrapolating the surface brightness profile to infinity. Col. (8): Total absolute B-band magnitude. Cols. (9)–(11): Average total colors for $(U-B)_T$, $(B-V)_T$, and $(V-R)_T$. Col. (12): B-band surface brightness within r_e. Cols. (13)–(15): Average colors within r_e for $(U-B)_e$, $(B-V)_e$, and $(V-R)_e$. Cols. (16)–(19): Color gradients outside of r_e (measured by finding the slope of the linear fit to the color profile for all good points outside of r_e) in units of Δmag per r_e for $(U-R)$, $(U-B)$, $(B-V)$, and $(V-R)$. A negative slope indicates that the galaxy becomes bluer with increasing radius, and a positive slope indicates that it gets redder outward. The second line for each galaxy lists errors for some quantities. The B_T error was derived from the total signal-to-noise ratio in the largest aperture measured. B_T(abs) errors also include the uncertainty on H_0 from *WMAP* measurements. Errors on the total and effective colors, $(X − Y)_T$ and $(X − Y)_e$, are the quadratic sum of the respective total X and Y magnitude errors. The $\mu_e(B)$ error is the accidental error derived from eq. (1). The errors on the color gradients were determined from the scatter of the fits. Table 4 is published in its entirety in the electronic edition of the *Astrophysical Journal*. A portion is shown here for guidance regarding its form and content.
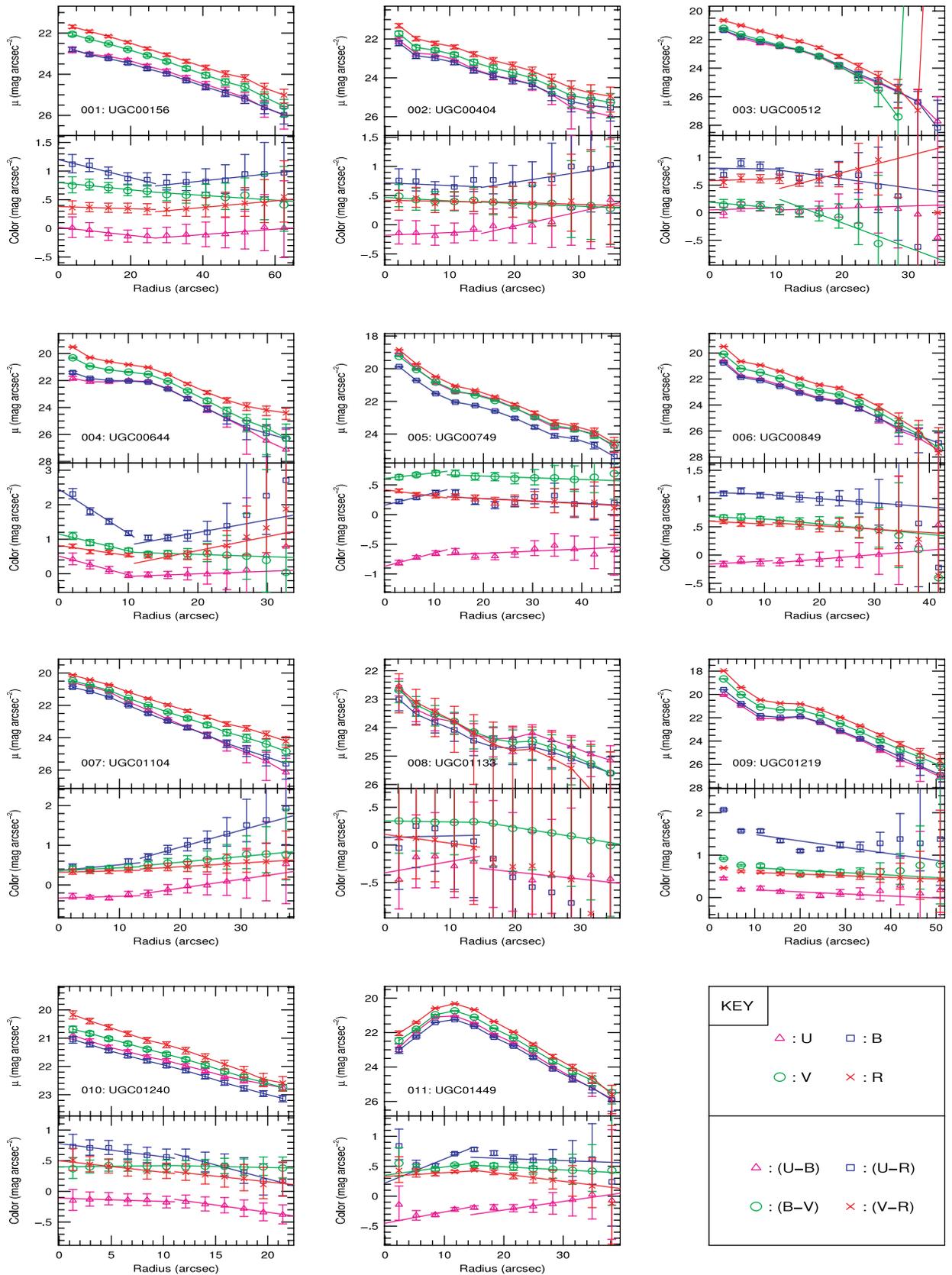
FIG. 5.—Surface brightness (μ) profiles (*top panels*) and color profiles (*bottom panels*) for each of the 142 galaxies imaged at the VATT. The lines in the color profile plots are the error-weighted linear least-squares fit to the data points inside r_e and outside r_e. No fit was made if there would be fewer than three good (signal-to-noise ratio above sky >0.5) points in the fit. [*See the electronic edition of the Journal for additional panels of this figure.*]
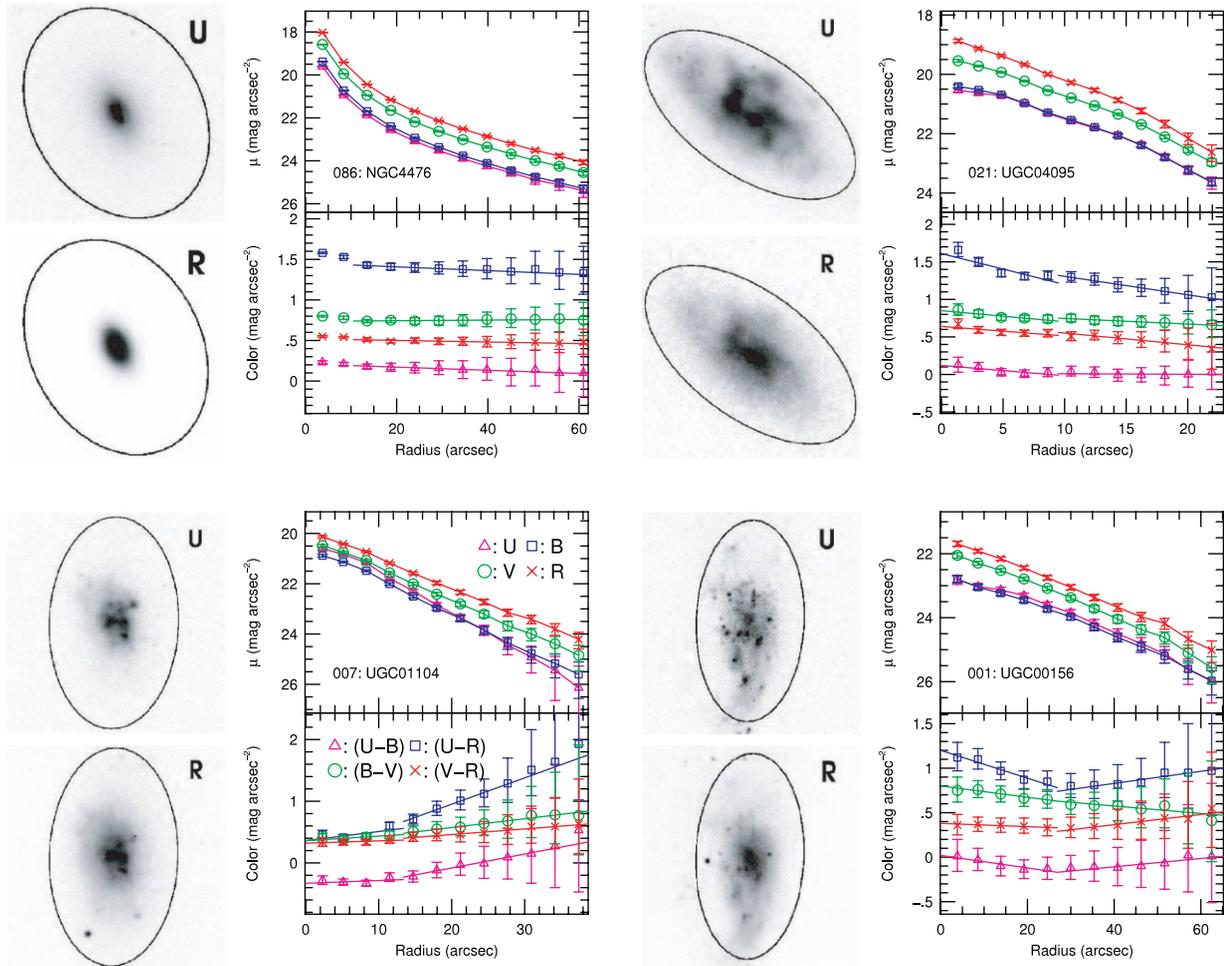
FIG. 6.—Examples of surface brightness (μ) and color profiles for some notable galaxies. The ellipses in the images mark the last annulus used in the profile calculation. Note that the images were scaled to highlight interesting galaxy structure, such that not all low surface brightness structure may be visible in these images. The top right panel for each galaxy is the surface brightness profile, and the bottom right panel is the color profile, with the same color legend as in Fig. 5. The key printed in the UGC 01104 plot applies to all of the plots. NGC 4476 is an early-type ($T = -1.0$) galaxy with constant to slightly bluer colors with increasing radius, which is typical of early-type galaxies. UGC 04095 is a mid-type ($T = 6.0$) spiral galaxy that also gets slightly bluer with radius, which is typical of mid-type galaxies. UGC 01104 is an irregular galaxy ($T = 10.0$) that gets redder with radius, which is more typical of late-type galaxies. UGC 00156 is a late-type spiral galaxy ($T = 9.3$) that actually gets bluer in the inner regions with radius but redder in the outer regions. This change in color gradient sign is common, occurring in about half of the galaxies in our sample.

is also no significant color gradient for early-type spiral galaxies (Sa–Sb), which at most get slightly redder with increasing radius (0.02 ± 0.05 mag arcsec^{-2} per r_e). Mid-type spiral galaxies (Sc) tend to get bluer with increasing radius by $1.8\,\sigma$ (-0.11 ± 0.06 mag arcsec^{-2} per r_e). This is also consistent with the findings in previous studies (de Jong 1996; Tully et al. 1996; Jansen et al. 2000; Bell & de Jong 2000; MacArthur et al. 2004). We see a significant ($\sim 3.6\,\sigma$) trend of redder colors with increasing radius for most of the late-type spiral and irregular galaxies, with a median color gradient of 0.25 ± 0.07 mag arcsec^{-2} per r_e for late-type spiral galaxies and a gradient of 0.27 ± 0.07 mag arcsec^{-2} per r_e for irregular galaxies. This suggests a distinction between the radial color gradient properties of elliptical and early to mid-type spiral galaxies (typically zero color gradients to a slightly bluer color with increasing radius, with some scatter between individual galaxies) and those of late-type spiral and irregular galaxies (typically redder color with increasing radius, with large scatter between individual galaxies). The peculiar and merger group ($T = 14$) becomes on average slightly redder with increasing radius (0.07 ± 0.03 mag arcsec^{-2} per r_e), although it has a large scatter in measured color gradients. This large scatter may be due to the particular physics of each galaxy interaction, since

widespread massive star formation can be triggered anywhere in such galaxies and results in either positive or negative color gradients. Dust may also play a role in reddening the inner parts of these galaxies, which would further decrease the color gradient. These two factors are particularly pronounced in currently merging galaxies and therefore may account for the more modest median color gradient we find for the interacting/merging group compared to the irregular galaxy group.

Figure 8 contains plots of the ($U - R$) outer color slope versus several other galaxy quantities derived from the RC3. Galaxies that did not have the relevant parameters listed in the RC3 were left out of the plot. The Hubble types from the RC3 show a similar trend with radial color gradient as our visual classifications (Fig. 7), with on average more galaxies becoming increasingly redder with increasing radius and a larger gradient scatter with increasing Hubble type. This same trend is seen with increasing major-axis diameter (which was converted to kpc using $H_0 = 71$ km s^{-1} Mpc^{-1}) and with increasing radial velocity with respect to the Galactic standard of rest, V_{GSR}. The former is not surprising, since later type galaxies tend to be intrinsically smaller than earlier type galaxies. The trend with radial velocity is likely due to Malmquist bias: since late-type galaxies tend to
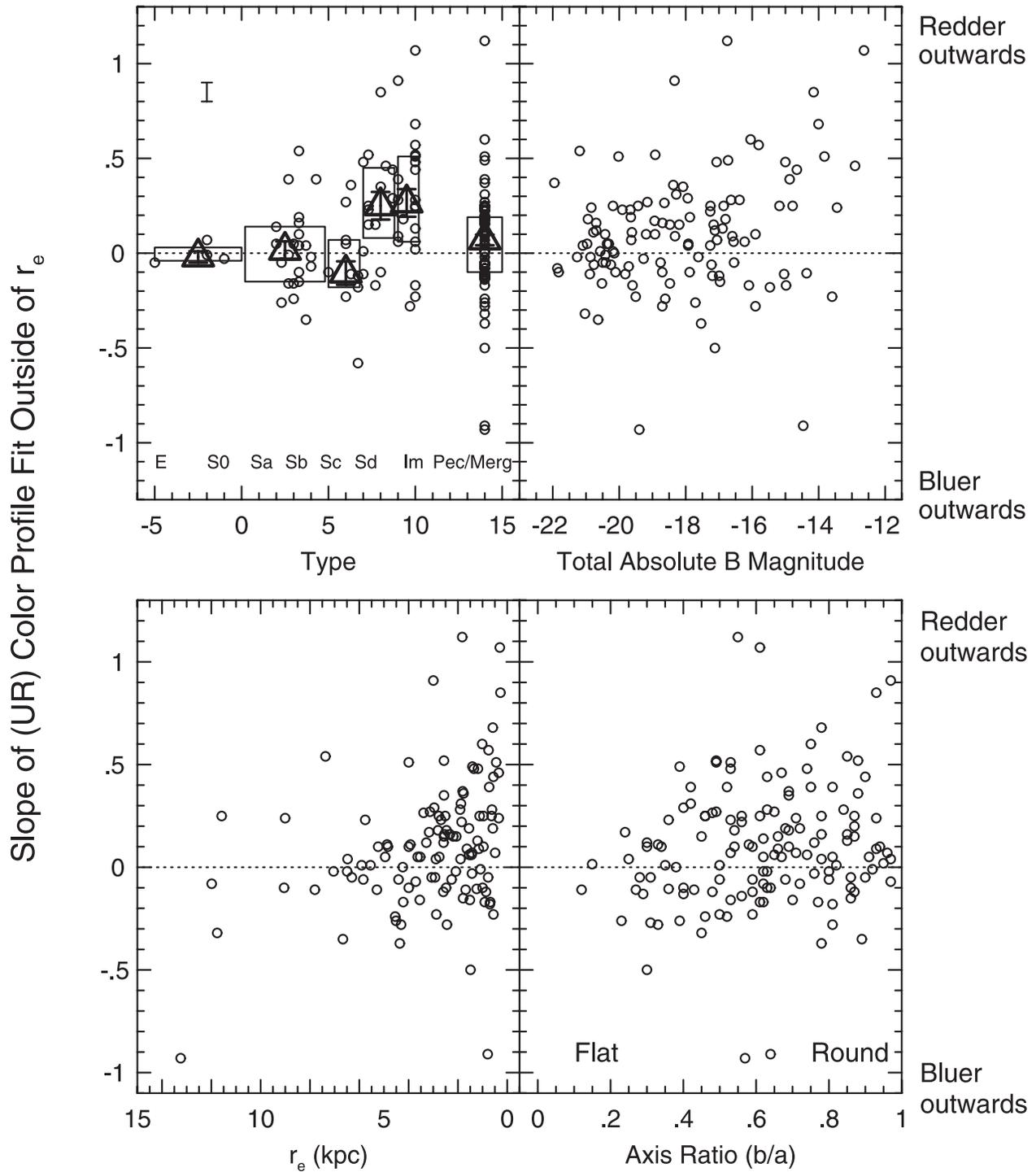
Fig. 7.—$(U - R)$ color gradient slope outside r_e (i.e., in the outer "disk") plotted against several galaxy parameters. The error bar in the upper left corner of the type panel (*top left*) shows the representative median error of the $(U - R)$ color gradient slope. The triangles in this panel represent the median color slope for several type bins. Boxes surrounding each median value enclose the type bin and the color slope 25% and 75% quartile ranges. Vertical error bars mark the errors on the medians. There is no significant median color slope within the errors for early-type (E–S0) galaxies or for early-type (Sa–Sb) spiral galaxies. Mid-type (Sc) spiral galaxies get slightly bluer with increasing radius, and late-type (Sd–Im) galaxies get significantly redder with increasing radius. Merger/peculiar galaxies get on average slightly redder with increasing radius, although they have a large range in color slopes. The scatter in this panel increases with increasing Hubble type, such that there is a wider range of possible color slopes with increasing type. The other panels show an average trend of fainter, smaller, and rounder galaxies (which tend to have later Hubble types) becoming increasingly redder with radius, with an increasingly larger range of possible slope values (larger scatter).

have a lower surface brightness than earlier types, they will be preferentially selected at nearer distances when using surface brightness–limited samples.

There is a weaker trend of increasingly redder outer regions with fainter B_T^0 (the absolute extinction-corrected total B-band

magnitude), M_{21} (the absolute H I 21 cm emission line magnitude), and, to a lesser extent, M_{FIR} (the absolute far-infrared magnitude). This trend is also seen with mean B-band surface brightness, μ_B, within r_e, although the low number statistics in this plot are due to the absence of effective radius (r_e) information for many
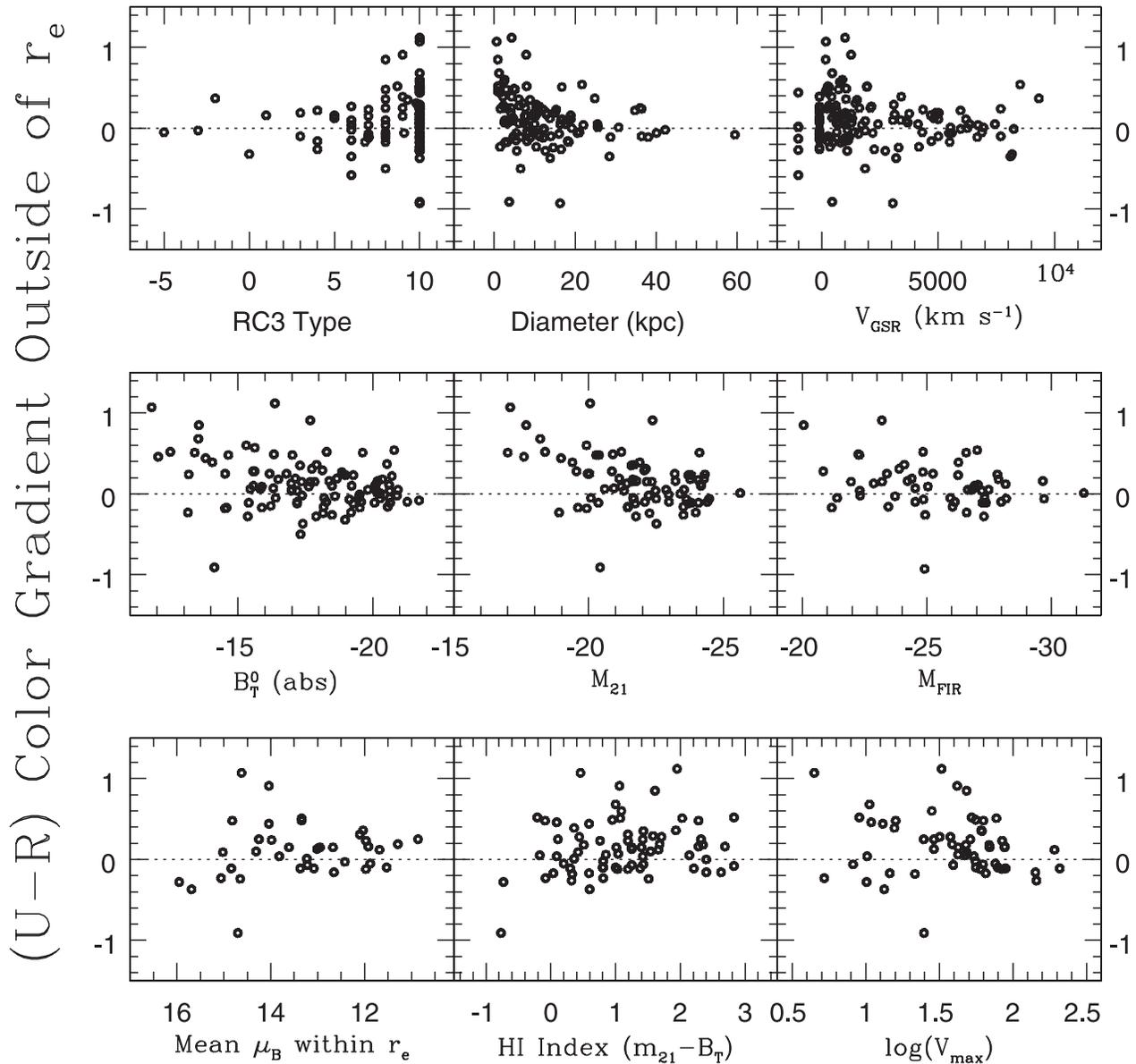
FIG. 8.—Radial $(U - R)$ color gradient slope vs. (*left to right, top to bottom*) RC3 Hubble type, major-axis diameter in kpc ($H_0 = 71$ km s^{-1} Mpc^{-1} for all calculations), radial velocity with respect to the Galactic standard of rest, extinction-corrected total absolute B magnitude, 21 cm emission line absolute magnitude, far-infrared (60–100 μm) absolute magnitude, mean B surface brightness within r_e, H I index equal to $(M_{21} - B_T^0)$, and the log of the maximum rotational velocity in km s^{-1}.

galaxies in the RC3. The H I index $[(M_{21} - B_T^0)$ color] does not display a strong trend with color gradient, even though it is apparent in B_T^0 and M_{21}. This suggests that galaxies that are overall intrinsically faint in all bands, which tends to be the case for late-type galaxies, have on average stronger gradients of redder colors with increasing radius, but that these are not necessarily caused by an excess of H I. This, coupled with the very weak trend seen in M_{FIR}, suggests that the increasingly redder outer regions of late-type galaxies may not be due to excess dust, but perhaps to other factors such as stellar population gradients. This is in agreement with the conclusions of other authors, who find that the observed color gradients for mid- to late-type galaxies are most likely due to stellar population effects (Vader et al. 1988; de Jong 1996; Jansen et al. 2000; Bell & de Jong 2000; MacArthur et al. 2004). It would be interesting to verify this with a thorough study of the spatial stellar population and dust content of late-type galaxies. There is no strong trend seen with log V_{max}, which is the log of the maximum rotational ve-

locity in km s^{-1} of the galaxy, although this is based on low number statistics due to the absence of this information for most of the galaxies in the RC3. The four galaxies with the largest V_{max}, however, have small color gradient slopes, which is consistent with the most massive galaxies being earlier type galaxies, which have been shown in multiple studies to have small color gradients with bluer regions typically at larger radii (Vader et al. 1988; Franx et al. 1989; Peletier et al. 1990).

These results raise the question of whether the late-type galaxies that get redder with increasing radius actually have redder colors in their outskirts than other galaxies (perhaps due to a particularly old stellar population in the outer disk or a radially increasing dust content) or whether they simply have uncommonly blue inner regions (perhaps due to younger or more metal-poor stars in the inner parts of the galaxy). Figure 9 addresses this with a plot of the $(U - R)$ color profile slope versus the total integrated $(U - R)$ color inside r_e ("bulge" color) and versus extrapolated $(U - R)$ color at $2r_e$ (outer "disk" color). Different
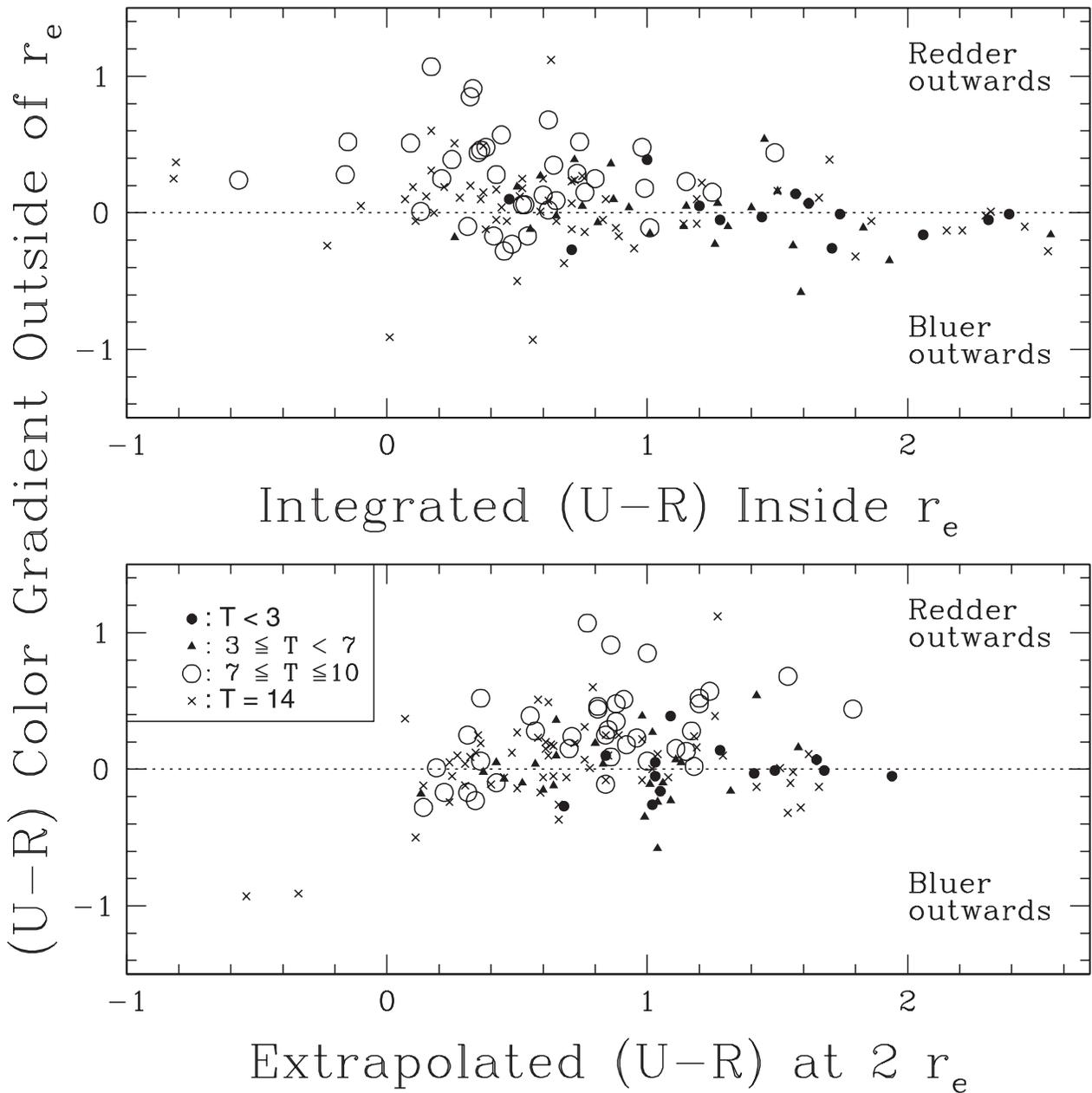
Fɪɢ. 9.—Radial $(U - R)$ outer color gradient slope vs. total inner $(U - R)$ color within r_e (*top*) and vs. outer disk color at $2r_e$ (*bottom*). Different type bins are indicated by different symbols. The early-type $(T < 3)$, mid-type $(3 \leq T < 7)$, and merger/interacting $(T = 14)$ galaxies do not show any significant trend in inner or outer color with color slope. Late Hubble type $(7 \leq T \leq 10)$ galaxies also show little trend in general, although as the galaxies get redder with increasing radius, they tend to be somewhat bluer in their inner regions *and* redder in their outer regions than other galaxies.

symbols represent different Hubble type bins. The early-type $(T < 3)$, mid-type $(3 \leq T < 7)$, and merger/interacting $(T = 14)$ galaxies do not show any significant trend in inner or outer color with color slope. Thus, the nonzero color gradients are not simply a mathematical artifact of these galaxies having an overall blue or red color but are a meaningful measure of a radial gradient in other physical properties of these galaxies. Late Hubble type $(7 \leq T \leq 10)$ galaxies also show little trend in general, although as these galaxies get redder with increasing radius, they tend to be bluer in their inner regions, *as well as* redder in their outer regions than other galaxies. *This suggests that, for late-type galaxies, most of the galaxies that get redder with radius are actually bluer in their inner regions* and *redder in their outskirts than late-type galaxies that get bluer with radius.* If this is due to stellar population differences (which is the favored

explanation of previous studies for color gradients) and not dust or other possible factors, this could be an indicator that late-type galaxies that get redder with increasing radius form from the outside in, with a relatively high amount of recent star formation in the inner regions (compared to other galaxies) and a relatively low amount of recent star formation in the outer regions.

4.2. HST Radial Color Gradients

Figure 10 shows all six *HST* surface brightness and color profiles with images of each galaxy in all three passbands. The ellipse on each image marks the outer annulus used for the last point in the profiles. NGC 3516 is an early-type galaxy $(T_{RC3} = -2.0)$ that becomes slightly bluer with radius in each of the colors $(F300W - F814W), (F300W - F160W),$ and $(F814W - F160W)$. NGC 2551, which is also an early-type galaxy $(T_{RC3} = 0.2)$,
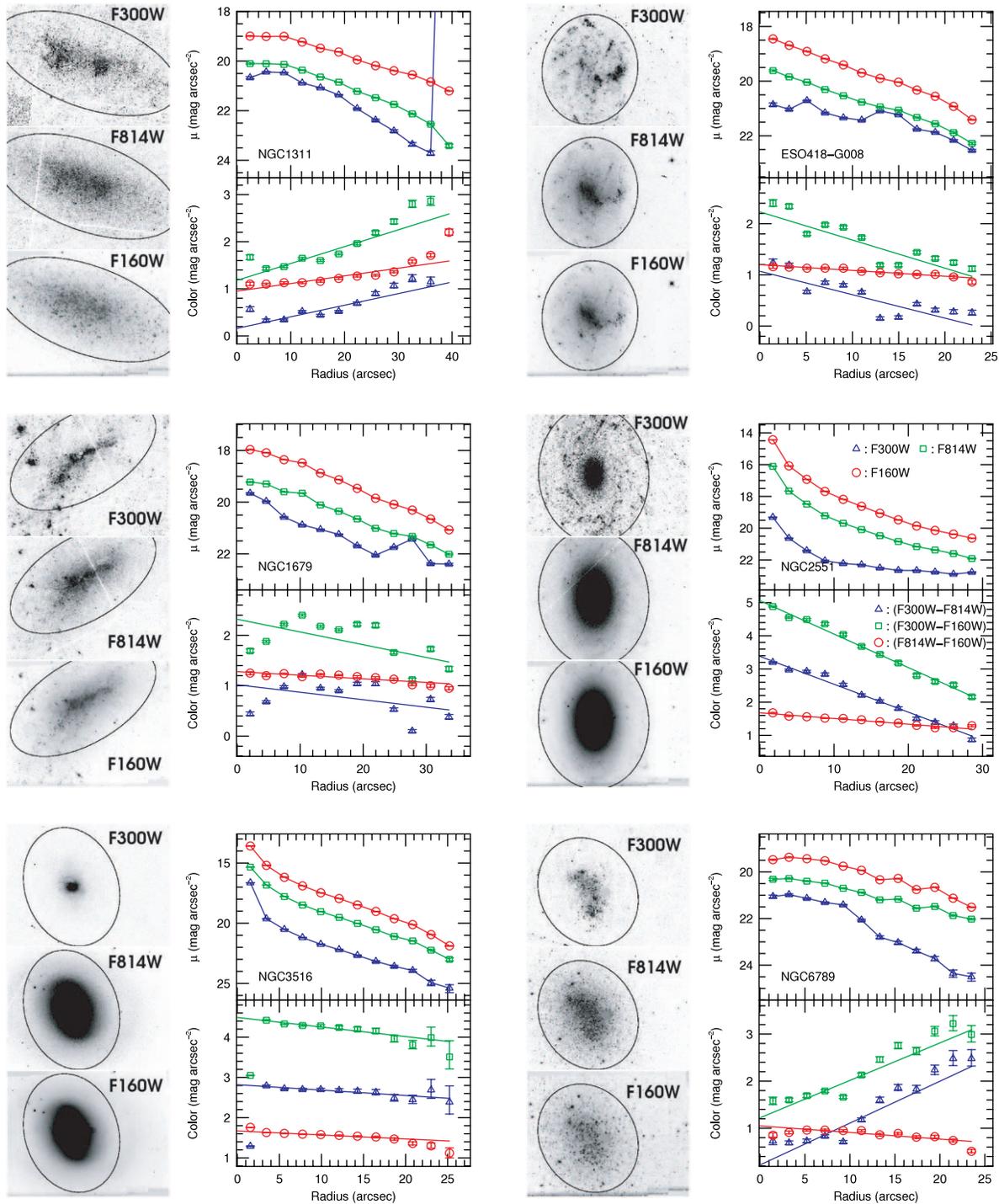
FIG. 10.—All six *HST* surface brightness (μ) and color profiles with images of each galaxy in all three passbands. The ellipse on each image marks the last annulus used in the profile calculation. Note that the images were scaled to highlight interesting galactic structure, such that existing low surface brightness material may not be visible in these images. The top right panel for each galaxy is the surface brightness profile, and the bottom right panel is the color profile. The key printed in the NGC 2551 plots applies to all of the plots. The lines in the color profile plots are the error-weighted linear least-squares fits to all of the data points.

gets significantly bluer with increasing radius in (F300W−F814W) and (F300W − F160W) but is fairly constant in color with radius in (F814W − F160W) (or, at most, gets slightly bluer with radius). NGC 1679 ($T_{RC3} = 9.5$) and ESO 418-G008 ($T_{RC3} = 8.0$) are late-type galaxies that get slightly bluer with increasing radius in all colors, which is true for half of the late-type galaxies. Of the other two late-type galaxies, NGC 6789 is an irregular galaxy ($T_{RC3} = 10$) that gets significantly redder with increasing radius in (F300W − F814W) and (F300W−

F160W) but gets slightly bluer with increasing radius in (F814W − F160W). NGC 1311 is a late-type Magellanic spiral (Sm) galaxy ($T_{RC3} = 9$) that gets redder with increasing radius in (F300W − F814W) and (F300W − F160W). It is the only one of these six galaxies that gets redder with increasing radius in (F814W − F160W).

We plot the color slopes for the six *HST* galaxies versus RC3 Hubble type in Figure 11. Due to small number statistics, broad conclusions cannot be confidently drawn from these results,
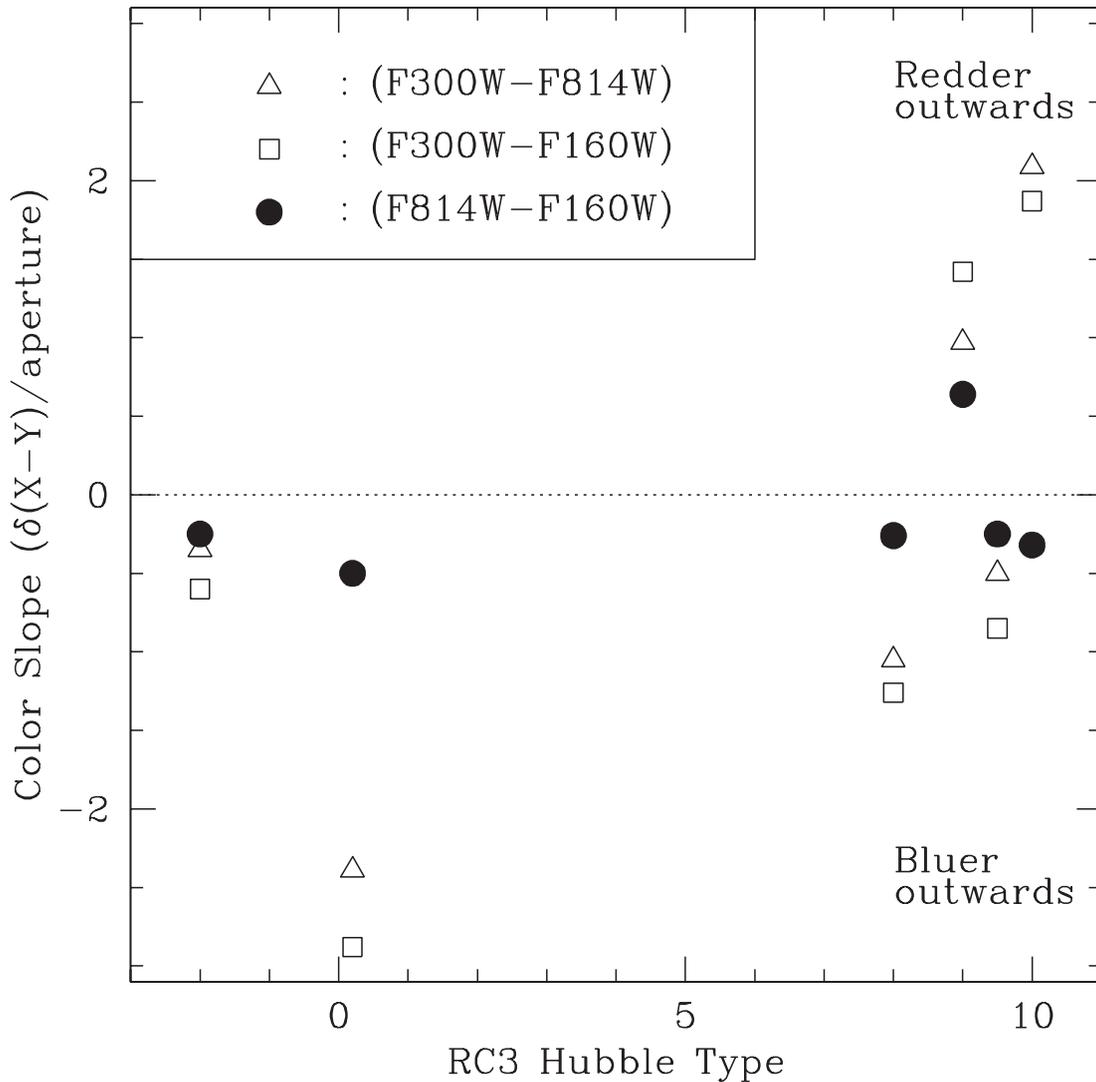
Fig. 11.—Color gradient vs. RC3 Hubble type for each of our *HST* galaxies. (F300W − F814W) and (F300W − F160W) gradients show a similar trend as the (U − R) gradients in the VATT data, with earlier galaxy types getting bluer with increasing radius and later galaxy types getting either bluer or redder with increasing radius. The (F814W − F160W) colors get slightly bluer with increasing radius for all but one galaxy (NGC 1311). For those galaxies that get bluer with radius in (F814W − F160W), the (F814W − F160W) gradients are roughly constant with Hubble type. Errors from the linear least-squares fit on the color slopes are comparable to the size of the symbols in this plot.

but it is encouraging to note that the (F300W − F814W) and (F300W − F160W) color gradients show similar trends as those of (U − R) in the VATT data, with earlier galaxy types getting bluer with increasing radius, and later galaxy types becoming either bluer or redder with increasing radius. Five out of the six galaxies get slightly bluer with increasing radius in (F814W − F160W). The magnitude of the (F814W − F160W) color gradient does not depend on Hubble type, at least for these five galaxies. This may not be a surprising result since the F 814W (8002 Å) and F160W (15,500 Å) filters do not sample significantly different portions of galaxy spectra. The only outlier is NGC 1311, which becomes significantly redder with increasing radius in (F814W − F160W). Comparison of the NGC 1311 images to the others reveals no inconsistencies in image quality that might cause this difference.

The F300W filter samples mid-UV light shortward of the atmospheric cutoff and the Balmer break, which contributes to color gradients that are sensitive to the presence of recent star formation. This may indicate that the redder outer parts of later Hubble type galaxies in (F300W − F814W) may be primarily

due to recent star formation concentrated near the center of these particular galaxy types. This young stellar population may exist among an underlying redder, older population that becomes more dominant toward the center of the galaxy, as evidenced by the bluer (F814W − F160W) color with increasing radius for most of the galaxies. The degenerate possibilities of increasing metallicity or dust toward the center of the galaxy may also explain the (F814W − F160W) gradients.

5. DISCUSSION

The bottom-up hierarchical structure formation model suggests that galaxies as they exist today were formed by the initial collapse of small mass fluctuations in the early universe, as well as the subsequent merging of these small systems into larger ones (e.g., White 1979; White & Frenk 1991; Cole et al. 1994; Kauffmann et al. 1997; Roukema et al. 1997; Baugh et al. 1998). In this formation model, galaxy mergers and interactions would be common factors in galaxy evolution. Mergers and interactions have been shown to trigger starbursts (e.g., Mihos & Hernquist 1994, 1996; Hernquist & Mihos 1995; Barnes & Hernquist 1996;

Somerville et al. 2001), which affect the radial color gradients of the galaxies. Starbursts can also be caused by bar instabilities (e.g., Noguchi 1988; Shlosman et al. 1989, 1990; Mihos & Hernquist 1994; Friedli & Benz 1993, 1995) or triggered by superwind shocks created by a combination of supernovae and winds from massive stars (e.g., De Young 1978; Dekel & Silk 1986; Mathews 1989; Heckman et al. 1990), but at high redshift, galaxy mergers and interactions should be the most common cause. In this case, mergers and interactions would funnel gas to the central regions of the galaxy and trigger nuclear starbursts. In the simplest picture, this would result in galaxies that recently underwent a merger or strong interaction becoming redder outward (Moth & Elston 2002). Many gas-rich interacting galaxies, however, show significant star formation in their outer parts, where tidal disturbances can trigger star formation. Dust in the interiors of these galaxies may also redden their colors. Thus, given the complexities of galaxy interactions and the large range in properties of the galaxies involved in such interactions, some galaxies that recently underwent an interaction will become redder while others will become bluer with increasing radius, consistent with our results.

If this overall picture of galaxy assembly is correct, then galaxies that more recently underwent a hierarchical merger or accretion event would be *more likely* to become redder than to become bluer with increasing radius than galaxies that have remained unperturbed and are substantially more relaxed today. Because the merger rate at high redshift is higher, higher redshift galaxies would on average be redder with increasing radius than lower redshift galaxies, and nearby low-mass, low-luminosity, late-type and interacting galaxies would on average be redder with increasing radius than their high-mass, high-luminosity, early-type counterparts that formed predominantly at higher redshift. This scenario can therefore be tested by examining how color gradients depend on galaxy type, luminosity, and redshift.

The process of galaxy formation may be more complicated, depending in part on the galaxy's type, luminosity, and mass and on its surrounding environment, as discussed by Tamura & Ohta (2003), who determined that elliptical galaxies in rich galaxy clusters get bluer with increasing radius and that larger and more luminous galaxies have steeper color gradients. These trends are consistent with models for formation through monolithic collapse (Eggen et al. 1962; Larson 1974; Carlberg 1984). In field E/S0 galaxies, there is no such strong trend of color gradient with galaxy luminosity and size, which suggests that early-type galaxies in less dense environments may form instead through hierarchical merging. Balcells & Peletier (1994) discuss the implications of early-type spiral galaxy bulge luminosity on the galaxy's formation process. They find that bright bulges show a steeper color gradient with increasing bulge luminosity, while faint bulges become significantly bluer outward and show no such color gradient relation with luminosity. This suggests that the brighter, more massive bulges in early-type spiral galaxies may have formed through dissipative collapse, with the presence of the disk having little effect on the bulge's formation. Fainter, less massive bulges, however, would have a different formation mechanism due to interactions with the disk (e.g., Kannappan et al. 2004).

Although the formation and evolution of specific galaxies may depend on various factors, our general results are consistent with the predictions of bottom-up hierarchical galaxy formation, where our more relaxed high-mass, high-luminosity, early- to mid-type galaxies either become bluer with increasing radius or have no color gradient, and our low-mass, low-luminosity, late-type galaxies tend to be redder on average with increasing ra-

dius. This is in agreement with trends seen in the high-redshift universe in the Hubble Deep Field–North by Moth & Elston (2002), who found that galaxies at intermediate redshifts ($z = 0.5–1.2$) tend on average to get bluer with increasing radius, while high-redshift galaxies ($z = 2–3.5$), which are expected to be experiencing more interactions and mergers, get on average redder with increasing radius. Moth & Elston (2002) determined that dust is unable to account for the strongly bluer central regions at high redshifts and that it must therefore be due to more centrally concentrated star formation. They argue that this can be explained by hierarchical galaxy formation models, which predict that mergers and interactions are important in galaxy evolution and more important at higher redshift. The resemblance of the color gradient trends in high-redshift galaxies to those of our late-type galaxies would be consistent with the apparent similarity in morphology between high-redshift galaxies and nearby irregular and peculiar galaxies. Therefore, the galaxies that most recently underwent mergers at both high and low redshift are the most likely ones to have color gradients that get significantly redder outward, reflecting this merger.

6. CONCLUSIONS

We have presented images and surface brightness and color profiles for 142 mostly late-type, irregular, and peculiar galaxies observed in *UBVR* at the VATT. Galaxies with Hubble types earlier than Sd tend to have small color gradients (if any) and become predominantly bluer outward, consistent with the conclusions of other authors (Vader et al. 1988; Franx et al. 1989; Peletier et al. 1990; de Jong 1996; Tully et al. 1996; Jansen et al. 2000; Bell & de Jong 2000; MacArthur et al. 2004). Our late-type spiral and irregular galaxies (Sd–Im), in contrast, on average tend to become significantly *redder* with increasing radius from their center. We find, however, that the scatter (range) in color gradients increases toward later Hubble type, such that one can find late-type galaxies that become somewhat bluer outward and late-type galaxies that become much redder outward. The largest range in color gradients is found among the peculiar/interacting/merging galaxies in our sample, most of which become slightly redder outward. This particularly large scatter is consistent with the large variety of galaxy morphological types included within this class of objects and with the complexity of the galaxy interactions.

We find that these color gradients do not have a significant dependence on the H I index, $(M_{21} - B_T^0)$, even though there is a trend of increasingly redder outer regions with fainter B_T^0 and fainter absolute H I 21 cm emission line magnitude, M_{21}. This suggests that galaxies that are faint in all bands (which tends to be true for late-type galaxies) do become on average redder with increasing radius, but these color gradients are not necessarily caused by an excess of H I. There is also a very weak trend of redder outer regions with fainter absolute far-infrared magnitude, M_{FIR}. Both of these results suggest that the increasingly strong gradients of redder colors with increasing radius in late-type galaxies may not be due to an excess of dust, but to other factors such as stellar population gradients. Other authors also conclude that these color gradients are most likely due to stellar population effects (Vader et al. 1988; de Jong 1996; Jansen et al. 2000; Bell & de Jong 2000; MacArthur et al. 2004). It would be interesting to verify this by means of a thorough study of the spatial distribution of dust in late-type galaxies.

We also analyze six galaxies observed with *HST* with NICMOS in F160W (*H*) and with WFPC2 in F300W (mid-UV) and F814W (*I*). The F300W data and, hence, the (F300W–F814W) and (F300W – F160W) color gradients are sensitive

to young stellar populations and star-forming regions. We find that the two earlier type galaxies become bluer with increasing radius in (F300W − F814W) and (F300W − F160W), while half of the four later type galaxies become bluer with increasing radius, and half become redder with increasing radius. Even though there are small number statistics, the fact that this trend resembles the trend seen in the larger ground-based sample suggests that these conclusions are reasonable. Color gradients measured from the (F814W − F160W) color profile show a different trend, with all but one galaxy becoming slightly bluer with increasing radius. These small color slopes, which seem to be roughly constant with Hubble type, may be due at least in part to the fact that F814W and F160W do not sample significantly different stellar populations. This and the sensitivity of F300W on star formation may also indicate that the redder outer parts of later type galaxies may be primarily due to recent star formation concentrated near the center of these particular galaxy types, even among an underlying redder, older population that becomes more dominate toward the center of the galaxy (or the degenerate possibilities of increasing metallicity or dust toward the center of the galaxy).

We propose that these color gradient trends are consistent with the trends predicted in hierarchical galaxy formation mod-els. The tendency of nearby irregular and peculiar/merging galaxies to become on average redder with increasing radius is similar to that of high-redshift galaxies. This lends some support to the theory that high-redshift galaxies are similar objects to the nearby irregular, peculiar, and merging galaxies that they resemble. A further, more detailed comparison of these nearby galaxies to high-redshift galaxies is needed to more fully understand the relationship between them, which we aim to address in a future paper (V. A. Taylor et al. 2005, in preparation).

REFERENCES

Abraham, R. G., Tanvir, N. R., Santiago, B. X., Ellis, R. S., Glazebrook, K., & van den Bergh, S. 1996, MNRAS, 279, L47
Balcells, M., & Peletier, R. F. 1994, AJ, 107, 135
Barnes, J., & Hernquist, L. 1996, ApJ, 471, 115
Baugh, C. M., Cole, S., Frenk, C. S., & Lacey, C. G. 1998, ApJ, 498, 504
Bell, E. F., & de Jong, R. S. 2000, MNRAS, 312, 497
Bertin, E., & Arnouts, S. 1996, A&AS, 117, 393
Bohlin, R. C., et al. 1991, ApJ, 368, 12
Cardiel, N., Gorgas, J., Sánchez-Blázquez, P., Cenarro, A. J., Pedraz, S., Bruzual, G., & Klement, J. 2003, A&A, 409, 511
Carlberg, R. G. 1984, ApJ, 286, 403
Cole, S., Aragon-Salamanca, A., Frenk, C. S., Navarro, J. F., & Zepf, S. E. 1994, MNRAS, 271, 781
de Grijs, R., Fritze-v. Alvensleben, U., Anders, P., Gallagher, J. S., Bastian, N., Taylor, V. A., & Windhorst, R. A. 2003, MNRAS, 342, 259
de Jong, R. S. 1996, A&A, 313, 377
Dekel, A., & Silk, J. 1986, ApJ, 303, 39
de Vaucouleurs, G., de Vaucouleurs, A., Corwin, H. G., Buta, R. J., Paturel, G., & Fouque, P. 1991, Third Reference Catalogue of Bright Galaxies (New York: Springer)
De Young, D. S. 1978, ApJ, 223, 47
Driver, S. P., Fernandez-Soto, A., Couch, W. J., Odewahn, S. C., Windhorst, R. A., Phillips, S., Lanzetta, K., & Yahil, A. 1998, ApJ, 496, L93
Driver, S. P., Windhorst, R. A., Ostrander, E. J., Keel, W. C., Griffiths, R. E., & Ratnatunga, K. U. 1995, ApJ, 449, L23
Eggen, O. J., Lynden-Bell, D., & Sandage, A. R. 1962, ApJ, 136, 748
Ellis, R. S. 1997, ARA&A, 35, 389
Eskridge, P. B., et al. 2003, ApJ, 586, 923
Ferguson, H. C., et al. 2004, ApJ, 600, L107
Franx, M., Illingworth, B., & Heckman, T. 1989, AJ, 98, 538
Friedli, D., & Benz, W. 1993, A&A, 268, 65
———. 1995, A&A, 301, 649
Giavalisco, M., Steidel, C. C., & Macchetto, F. D. 1996, ApJ, 470, 189
Glazebrook, K., Ellis, R., Santiago, B., & Griffiths, R. 1995, MNRAS, 275, L19
Heckman, T. M., Armus, L., & Miley, G. K. 1990, ApJS, 74, 833
Hernquist, L., & Mihos, J. 1995, ApJ, 448, 41
Hibbard, J. E., & Vacca, W. D. 1997, AJ, 114, 1741
Hill, J. K., et al. 1992, ApJ, 395, L37
Holtzman, J. A., Burrows, C. J., Casertano, S., Hester, J. J., Trauger, J. T., Watson, A. M., & Worthey, G. 1995, PASP, 107, 1065
Jansen, R. A., Franx, M., Fabricant, D., & Caldwell, N. 2000, ApJS, 126, 271

Kannappan, S. J., Jansen, R. A., & Barton, E. J. 2004, AJ, 127, 1371
Kauffmann, G., Nusser, A., & Steinmetz, M. 1997, MNRAS, 286, 795
Kuchinski, L. E., et al. 2000, ApJS, 131, 441
Landolt, A. U. 1992, AJ, 104, 340
Larson, R. B. 1974, MNRAS, 169, 229
Lowenthal, J. D., et al. 1997, ApJ, 481, 673
MacArthur, L. A., Courteau, S., Bell, E., & Holtzman, J. A. 2004, ApJS, 152, 175
Marcum, P. M., et al. 2001, ApJS, 132, 129
Mathews, W. 1989, AJ, 97, 42
Mihos, J., & Hernquist, L. 1994, ApJ, 425, L13
———. 1996, ApJ, 464, 641
Milliard, B., Donas, J., Laget, M., Armand, C., & Vuillemin, A. 1992, A&A, 257, 24
Monet, D., et al. 1996, USNO-A2.0 (Washington DC: US Naval Obs.)
Moth, P., & Elston, R. J. 2002, AJ, 124, 1886
Noguchi, M. 1988, A&A, 203, 259
Odewahn, S. C., Cohen, S. H., Windhorst, R. A., & Philip, N. S. 2002, ApJ, 568, 539
Odewahn, S. C., Windhorst, R. A., Driver, S. P., & Keel, W. C. 1996, ApJ, 472, L13
Peletier, R. F., Davies, R. L., Illingworth, G. D., Davis, L. E., & Cawson, M. 1990, AJ, 100, 1091
Persson, S. E., Frogel, J. A., & Aaronson, M. 1979, ApJS, 39, 61
Rhoads, J. E. 2000, PASP, 112, 703
Roukema, B. F., Quinn, P. J., Peterson, B. A., & Rocca-Volmerange, B. 1997, MNRAS, 292, 835
Sandage, A. 1972, ApJ, 176, 21
Shlosman, I., Begelman, M. C., & Frank, J. 1990, Nature, 345, 679
Shlosman, I., Frank, J., & Begelman, M. C. 1989, Nature, 338, 45
Somerville, R., Primack, J. R., & Faber, S. M. 2001, MNRAS, 320, 504
Tamura, N., & Ohta, K. 2003, AJ, 126, 596
Taylor, V. A., Jansen, R. A., & Windhorst, R. A. 2004, PASP, 116, 762
Tinsley, B. M., & Larson, R. B. 1978, ApJ, 221, 554
Trujillo, I., et al. 2004, ApJ, 604, 521
Tully, R. B., Verheijen, M. A. W., Pierce, M. J., Huang, J., & Wainscoat, R. J. 1996, AJ, 112, 2471
Vader, J. P., Vigroux, L., Lachieze-Rey, M., & Souviron, J. 1988, A&A, 203, 217
White, S. D. M. 1979, MNRAS, 189, 831
White, S. D. M., & Frenk, C. S. 1991, ApJ, 379, 52
Windhorst, R. A., et al. 2002, ApJS, 143, 113